

**UNIVERSITY OF CALIFORNIA,
IRVINE**

Gold/PolyPyrrole Actuators for active Micromixing

THESIS

Submitted in satisfaction of the requirements
for the degree of

MASTER OF SCIENCE

in Chemical and Biochemical Engineering

by

Xavier Casadevall i Solvas

Thesis Committee:
Professor Marc Madou, Chair
Professor Andrew Putnam
Professor Henry Lim

2007

The thesis of Xavier Casadevall i Solvas is approved:

Committee Chair

University of California, Irvine
2007

DEDICATION

To

Each one of the persons that in one way or another
have helped me to make this thesis possible.

TABLE OF CONTENTS

1	Introduction.....	1
2	Background.....	2
2.1	Micromixing applications.....	2
2.2	The Physics of Micromixing.....	3
2.3	Micromixing strategies.....	10
2.4	Au/PPy Actuators.....	15
2.5	Electrochemical measurements.....	18
2.6	Electromagnetic interference.....	26
3	Objectives.....	29
3.1	Sensor near flap (<i>SnF</i>).....	29
3.2	Sensor on flap (<i>SoF</i>).....	30
3.3	Micro Sensor near flaps (<i>mSnF</i>).....	32
4	Experimental Work.....	34
4.1	Device Fabrication.....	34
4.1.1	Masks Fabrication.....	35
4.1.2	Sensor near flap (<i>SnF</i>).....	35
4.1.3	Sensor on flap (<i>SoF</i>).....	37
4.1.4	Micro Sensor near flaps (<i>mSnF</i>).....	38
4.2	Flaps Actuation.....	39
4.3	Electrochemical experiments.....	39
4.3.1	Current-Potential (i-E) Experiments.....	40
4.3.2	ChronoAmperometric Experiments.....	41
4.3.3	Interference analysis and data filtering method.....	42
4.4	Flap Movement visualization and recording.....	45
5	Results and Discussion.....	47
5.1	Fabrication results.....	47
5.1.1	Sensor near Flap (<i>SnF</i>).....	47
5.1.2	Sensor on Flap (<i>SoF</i>).....	47
5.1.3	Micro sensor near Flaps (<i>mSnF</i>).....	51
5.2	Flaps Actuation.....	52

5.2.1	Effect of Flap dimensions on Motion	52
5.2.2	Input Function effect on Flap position	53
5.2.3	Flap motion model	54
5.2.4	Time and applied function effects on Flap motion	55
5.2.5	Flap motion in the devices tested	56
5.3	Electrochemical experiments	58
5.3.1	Notes on experimental set-up.....	58
5.3.2	Current-Potential (i-E) Experiments	59
5.3.3	ChronoAmperometric Experiments	59
5.3.3.1	Diffusion-limited Blank and Noise Blank experiments.....	60
5.3.3.2	Mixing experiments	65
6	Conclusions	76
7	Future Work	77

LIST OF FIGURES

<p>Figure 1: 1 and 2 hinges swimming micro-structures..... 6</p> <p>Figure 2: Laminar Fluid flowing around a plate 8</p> <p>Figure 3: Turbulent Fluid flowing around a plate 9</p> <p>Figure 4: T-mixer 11</p> <p>Figure 5: H-filter 12</p> <p>Figure 6: Staggered herringbone mixer 14</p> <p>Figure 7: Examples of Active mixers 15</p> <p>Figure 8: PPy backbone structure 16</p> <p>Figure 9: Au/PPy actuator 18</p> <p>Figure 10: Electrical equivalent circuit to two electrodes in solution 19</p> <p>Figure 11: Potential source and Amperometer coupled with two electrodes in solution and equivalent circuit 20</p> <p>Figure 12: Nonfaradic current response after a Potential step experiment 20</p> <p>Figure 13: Equilibrium potential (E) definition 22</p> <p>Figure 14: Reduction process when η is decreased with respect to E..... 23</p> <p>Figure 15: ChronoAmperometric experiments at different applied overpotentials 24</p> <p>Figure 16: Construction of a Sampled current voltammetry or i-E curve..... 25</p>	<p>Figure 17: Example of Capacitive Coupling 27</p> <p>Figure 18: Example of Inductive Coupling 28</p> <p>Figure 19: Sensor near Flap configuration..... 29</p> <p>Figure 20: Dimensions of SnF fabricated devices 30</p> <p>Figure 21: Sensor on Flap Configuration..... 31</p> <p>Figure 22: Dimensions of SoF fabricated devices 31</p> <p>Figure 23: Configurations and Dimensions of mSnF fabricated devices 33</p> <p>Figure 24: Fabrication process for SnF and mSnF 34</p> <p>Figure 25: Fabrication process for SoF 34</p> <p>Figure 26: Undercut effect on Polyimide when developing PR. 36</p> <p>Figure 27: Scheme of the electrochemical and flap-actuation experimental set-up..... 40</p> <p>Figure 28: Typical Diffusion-limited response of several ChA experiments 41</p> <p>Figure 29: Ideal behaviour of the EMI and Redox interferences, which could be filtered by a numerical method capable of removing periodical components..... 43</p>
--	--

Figure 30: Numerical method for removal of periodic perturbations on an underlying signal.....	44	Figure 42: i-E curve for $\text{Fe}(\text{CN})_6^{4-}$ in PBS	59
Figure 31: Set-up for the mSnF experiments	46	Figure 43: Noise Experiment for a SnF device.....	61
Figure 32: SnF devices.....	47	Figure 44: Noise Experiment for a SoF device.....	62
Figure 33: Fabrication strategies for thick and thin electronically insulating layers	49	Figure 45: Noise Experiment for a mSnF device	63
Figure 34: SoF device	49	Figure 46: Mixing experiments for a SnF (10x0.5mm).....	66
Figure 35: Undercut problems in thin Polyimide Insulating layers.....	50	Figure 47: Mixing experiments for a SnF (5x0.25mm).....	67
Figure 36: Undesired PPy growth on sensor area.....	51	Figure 48: Mixing experiments for a SoF (10x0.5mm).....	69
Figure 37: PPy deposition process examples.....	52	Figure 49: Mixing experiments for a mSnF (2 On-Phase Flaps).....	70
Figure 38: Secondary “Twisting” and “Corckscrew” motions	54	Figure 50: Mixing experiments for a mSnF (6 On-Phase Flaps).....	71
Figure 39: Flap motion model.....	55	Figure 51: Mixing experiments for a mSnF (3vs3 Flaps).....	72
Figure 40: Effects of time and applied function on the motion of the flaps ...	56		
Figure 41. Movement of a SoF device with 3 μm thick Polyimide insulating layer.....	57		

ACKNOWLEDGEMENTS

I would like to start giving many thanks to the director of my Master's Thesis, Prof. Marc J. Madou, for giving me the opportunity to work on this exciting topic.

I would also like to thank the "California-Catalonia Engineering innovation program", which funded this project for year 2006, and specially its director, Prof. Roger Rangel.

I finally want to express my gratitude to Anthony Tsai, Han Xu and Dr. Lawrence Kulinsky, for many clarifying discussions and advice.

ABSTRACT OF THE THESIS

Gold/PolyPyrrole Actuators for Active Micromixing.

By

Xavier Casadevall i Solvas

Master of Science in Chemical and Biochemical Engineering

University of California, Irvine, 2007

Professor Marc J. Madou, Chair.

This Thesis presents the work done in the area of *Active Micromixing* using Gold/PolyPyrrole (Au/PPy) actuators. These actuators are bilayer structures that take advantage of changes in Volume of the PPy when certain voltages are applied on it due to ion exchange between the Polymer matrix and an ionic solution. This changes in volume of the PPy, translate to a bending movement of the Au/PPy structure.

In combination with an electrochemical technique specially designed to only respond to mass transport effects in a fluid around a sensor, different configurations of Au/PPy actuators and sensors were tested with different spacial positioning. The aim was to study the effect that the moving structures would have on the fluid surrounding the sensor and on the mass transport related response observed on it. For this purpose Diffusive-limited mass transport experiments (where the actuators were not activated) were run and compared to experiments where these actuators were in motion.

Results show that, under certain experimental limitations, *Active Micromixing* was achieved and so an increase with respect to the Diffusive-limited mass transport was observed on systems with moving actuators.

1 Introduction

Recent advances in microfabrication techniques have led to many different areas of research related to chemistry (chemical and biochemical sensing applications), medicine, and biology (drug delivery, drug discovery, proteomics, and genomics) [1,2].

The possibility to fabricate sensors, fluidic systems, power and heat sources, and other machinery on micron scale has led to the realization that many analytical and experimental techniques commonly used in the fields of chemistry, biology, and medicine could be miniaturized, and as a consequence made less expensive, faster, and have better resolution compared to some standard macro-scale technologies.

A field of research known as “*Lab-on-a-Chip*” [3] is composed of many different application areas (micro-fluidics, micro-mechanics, micro-electronics), all of which need to be integrated for the success of any future new applied technologies.

In this document we present our efforts made in the area of micro-fluidics with the particular goal of fabricating and testing a new design for *Active Micromixing* applications.

2 Background

2.1 Micromixing applications

Mixing is a particularly interesting process on the microscale, with a wide variety of applications.

Many liquid-phase chemical and biological processes exhibit dynamics that cannot be resolved in reaction kinetics experiments because they are faster than the mix times of conventional mixers. Protein folding is one important example in which the current emphasis is on time scales shorter than the millisecond mixing times attainable with traditional, stopped-flow methods [4]. The fastest mixers used for reaction kinetics introduce turbulence by forcing reactant streams at high velocity through a nozzle, yielding mixing times below 100 μs , but this process is inherently difficult to control and it consumes large volumes of sample. The transit time of the mixed fluid through the nozzle further imposes a dead time during which the reaction is obstructed from view. A faster alternative to turbulent mixing is to reduce the length scale over which the fluids must diffusively mix by microfabricating the nozzles [5].

Chemical and Biochemical sensing techniques for particular applications (like gene expression profiling and high throughput screening), require multiplexing and rapid homogeneous mixing of macromolecular solutions, such as DNA or globular proteins. Mixing of macromolecular solutions by molecular diffusion may take considerable time (dozens of minutes), and diffusion-limited reactions can take several hours (depending on the reactive species properties and concentration). Micromixing has been shown to substantially speed up some biochemical reactions [6, 7]. For applications where only a very small concentration of analyte is available (and so

diffusion takes place very slowly), effective micromixing strategies are the key parameter to reduce assay times.

Many other applications for mixing on the microscale were recently reviewed in the literature [8-10].

2.2 The Physics of Micromixing

By “*mixing*” we refer to the process of homogenization of the mass-related physical characteristics (concentration, density, viscosity) of two or more fluids that initially possessed different characteristics (or even different phases), so that by the end of this process the initial fluids can no longer be differentiated, and we can recognize only a single homogeneous fluid with continuous characteristics.

The process of mixing is (in the absence of electromagnetic fields and external forces) essentially due to the Brownian motion, the net effect of which is formalized by Fick’s 1st and 2nd laws (equations. (1) and (2)):

$$\mathbf{J}_A = -D_A \nabla C_A \quad (1); \quad \frac{\partial C_A}{\partial t} = D_A \nabla^2 C_A \quad (2)$$

These expressions relate the Flux of species A (\mathbf{J}_A) and the variation of its concentration (C_A) over time with a Diffusivity Coefficient (D_A) and with its spacial variation in concentration. As can be seen from equation (1) the flux of molecules A will be from regions of higher to regions of lower concentration.

It is very common to find expressions such as “*convective mixing*” or “*turbulent mixing*”. This terminology applies when not only Diffusion, but also other processes (like *Stirring*) take place. The mechanical process of *Stirring* can increase *mixing* by

producing interdigitated regions of different characteristics, and thus reducing the distance through which molecules diffuse to homogenize the solution.

It is also important to introduce at this point the equations of continuity (mass conservation) and motion (momentum conservation) for incompressible Newtonian fluids - equations (3) and (4) respectively:

$$(\nabla \cdot \mathbf{v}) = 0 \quad (3); \quad \frac{\partial}{\partial t} \rho \mathbf{v} = -[\nabla \cdot \rho \mathbf{v} \mathbf{v}] - \nabla P + \mu \nabla^2 \mathbf{v} + \rho \mathbf{g} \quad (4)$$

Eq. (3) simply states that there is no variation in the density of the fluid. Eq. (4), known as Navier-Stokes equation, states that momentum flux change in a fluid is a function of the inertial, pressure, viscous, and gravitational forces exerted on this fluid (right-hand-side terms).

The relationship between the Viscous and the Inertial forces that act upon a specific fluid in motion can be described by the dimensionless Reynolds number,

$$\text{Re} = \frac{u_0 L_0}{\nu} \quad \text{or also} \quad \text{Re} = \frac{\text{Inertial}}{\text{Viscous}} \quad (5)$$

where u_0 is the characteristic velocity of the fluid, L_0 is the characteristic length of the channel/vessel/obstacle and ν is the kinematic viscosity.

Flows in pipes at Reynolds numbers above 3000 are defined as turbulent (inertial forces dominate), and flows below 2300 are defined as laminar (viscous forces are dominant). Turbulent flow is characterized by unpredictable fluid motion with unstable velocity profiles. Laminar flows, on the other hand, have characteristically well defined velocity profiles and stream and path lines.

When *mixing* two initially separated fluids, a major difference between turbulent and laminar flows can be immediately observed: the random velocity configurations of

the turbulent flow promote a faster and more intimate contact between sections of the initially separated fluids. Therefore, the distance between regions of each fluid section is reduced and so Diffusion takes place more rapidly (as stated in Fick's laws). On the other hand, in laminar flows where interdigitation of initially separated sections of the fluids does not occur, distances between sections are longer, and so Diffusion of the different species happens more slowly.

With water as the typical working fluid, typical velocities of 1 $\mu\text{m/s}$ – 1 cm/s , and typical channel radii of 1–100 μm , the Reynolds numbers range between 10^{-6} and 10. These low Reynolds values affirm that viscous forces typically dominate inertial forces in micron-size devices, and the resulting flows are almost always laminar. Hence, the practical advantages of promoting turbulence for enhancing any given *mixing* process cannot be easily achieved on the microscale.

Under extreme circumstances (very slow steady flow), Eq (4) can be rewritten as

$$-\nabla P + \mu \nabla^2 \mathbf{v} + \rho \mathbf{g} = 0 \quad (6)$$

which is also known as “Stokes Flow” or “Creeping Flow” equation, typical of the microscopic domain, where inertial forces and unsteady terms are neglected.

In the beginning of this chapter we introduced Fick's laws of Diffusion, as the fundamental mechanism of *mixing*. It is also important to introduce a more detailed expression for *Mass Transport*, when, in addition to concentration gradients, flow and electric fields are also present:

$$\mathbf{J}_A = -D_A \nabla C_A - \frac{z_A F}{RT} D_A C_A \nabla \phi + C_A \mathbf{v} \quad (7)$$

The second term of this expression stands for “*Migration*” (electrically driven transport of charged particles) and the last term stands for “*Convection*” (mass transport due to flow or inertial motion of the particles).

In some systems, as we will see below in part 2.5, some of these phenomena can be eliminated or made negligible so that some parameters (concentration, velocity field, Diffusivity coefficient, etc.) of a solution can be studied closely. In the particular case of the experiments that will be presented in this work, a *Diffusion*-based system in which *Convection* is promoted with an actuated device, is used to gain some insight about the *mixing* capabilities of the system under study.

An interesting issue regarding flow or movement of particles at very Low Reynolds numbers was presented in the paper by E. M. Purcell, [11]. When discussing how microorganisms can effectively “swim” in low **Re** fluids, Purcell presents the theoretical examples given in Figure 1.

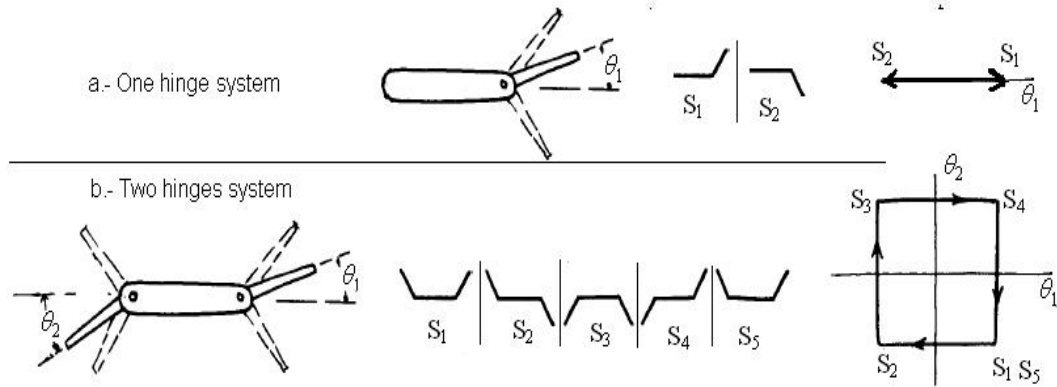


Figure 1: 1 and 2 hinges swimming micro-structures [11]

In case *a*, as discussed in the paper, the device is bound to move back and forth to the same initial and final positions (S_1 and S_2). In case *b*, the device can move in a loop (or even more complicated trajectories), covering a larger distance (from S_1 to S_5). This idea is precisely what makes the devices presented in section 3.3 interesting,

because it implies that it is physically possible to move portions of fluid even at extremely low **Re** when more than one actuating hinge is active.

It is also important to present a brief introduction of the Boundary Layer Theory (BLT) that describes Momentum and Mass transfer in the vicinity of physical boundaries (walls and other objects). As size of the system decreases, the near-boundary regions will occupy more and more volume relative to the bulk of the solution. For micron- and submicron-size systems BLT becomes an essential tool.

Let's consider a plate (of length L) surrounded by a motionless fluid occupying an infinite space that has a fixed Bulk concentration of species A (C_A^*). If the concentration on the surface of the plate, due to a consuming reaction, is maintained at $C_{A0} = 0$, this difference in concentration will promote a Diffusive mass transfer from regions of higher concentration to the plate surface. This will create a region near the plate surface where the concentration of species A will range from C_A^* to 0. This region is called *Diffusion Boundary layer* and its thickness δ varies over time according to the following expression:

$$\delta \simeq \sqrt{\pi D_A t} \quad (8)$$

Consider the same case, but now with the fluid moving (Figure 2) with a constant velocity (v_m) in the Laminar regime.

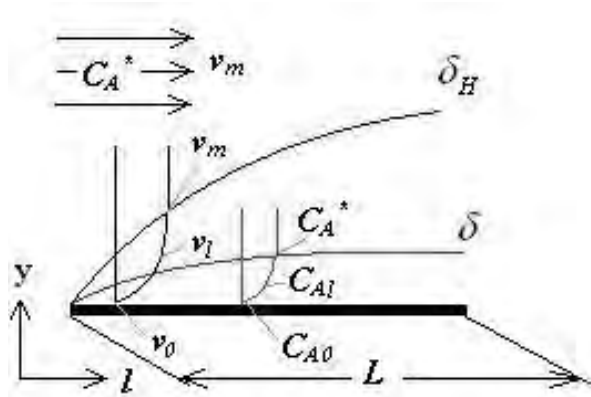


Figure 2: Laminar Fluid flowing around a plate

The “No-slip” boundary condition of the flow at the surface of the plate promotes a new region where the velocity of the fluid ranges from $v_0 = 0$ at the very surface of the plate to v_m , at a certain distance δ_H . This region is called the *Velocity Boundary layer*, and its thickness (δ_H) is expressed as:

$$\delta_H \approx \sqrt{\frac{\nu l}{v_m}} \quad (9)$$

Under this new flow conditions, mass transport occurs not only by Diffusion but also by Convection. It is common to combine the convective and diffusive terms of the *Mass transfer equation*, eq. (7). In this case a new expression for the *Diffusion Boundary layer* thickness (reduced because of Convection) is used:

$$\delta \approx D_A^{1/2} \nu^{1/6} \left(\frac{l}{v_m} \right)^{1/2} \quad (10)$$

For this particular case the relationship between the thicknesses of the *Diffusion Boundary layer* and the *Velocity Boundary layer* is:

$$\delta = \left(\frac{D_A}{\nu} \right)^{1/3} \delta_H \quad (11)$$

This has been presented as an example to introduce the reader to the concept of the *Diffusion Boundary layer* and how Convection can affect it. Other flows (constrained between parallel plates, in pipes, etc.) would have different characteristic *Velocity* and *Concentration Boundary layer* profiles. As an example, the same case study in a Turbulent regime (like the initially presented laminar flow with larger L and v_m), would require a different mathematical treatment, and the profile of the Velocity Boundary layer near the plate would have the following shape (Figure 3).

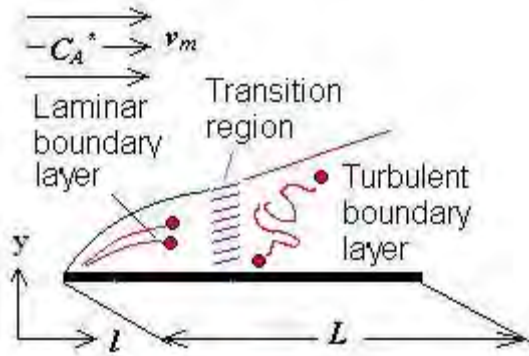


Figure 3: Turbulent Fluid flowing around a plate

Also a brief description on “Chaotic dynamics” will be introduced. Particles moving with a fluid in motion are considered to have the same velocity than the fluid, as expressed in the following equations.

$$\mathbf{V}_{particle} = \mathbf{V}_{fluid} \quad \begin{aligned} \frac{dx}{dt} &= u(x, y, z, t) \\ \frac{dy}{dt} &= v(x, y, z, t) \\ \frac{dz}{dt} &= w(x, y, z, t) \end{aligned} \quad (12)$$

This system of equations, depending on the expressions of u , v and w (velocity profiles of the fluid obtained from Navier-Stokes), can be non-integrable, and so the

movement of particles in the flowing fluid (*Advection*) can be *Chaotic*. The velocity field of the fluid, which can even be steady for 3-D cases, doesn't even have to be very complex for these system to be dynamically *Chaotic*.

2.3 Micromixing strategies

Traditionally there has been a differentiation between the so-called *Passive* and *Active mixers*. *Passive mixers* are made out of fixed elements that do not require external energy (other than that which is necessary to promote the flow). They rely on *Diffusion* and *Chaotic advection*¹ for mixing. Some examples of these Passive mixers are given below.

We have already introduced the issue of the laminarity of the flow in the microscale systems, and also the theoretical constraints to create turbulence and thus convectively enhance *mixing* (or diffusive mass transport) in microfluidic devices. Hence, the traditional approach implemented in micro-fluidics has been to increase diffusive mass transport by reducing the length across which a species needs to diffuse in order to produce a homogeneous solution. Many examples of these approaches have been implemented and can be found in the literature [12-19]. A traditional microfluidic device [12] is the so-called *T mixer* or *T sensor* (Figure 4).

¹ Chaotic particle motion in fluids, even in fluids under laminar flow, as defined in [20]

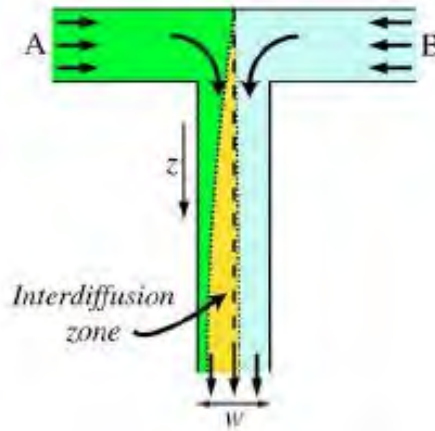


Figure 4: T-mixer

With this concept it is possible to mix different fluids. But how far down the channel must the fluids flow before the channel is homogenized? A simple estimate requires the particles or molecules to diffuse across the entire channel, giving a time $\tau_D \sim w^2/D$, where w is the width of the channel and D is the Diffusivity Coefficient. During this time, a fluid stripe would have moved a distance $Z \sim U_0 w^2/D$ down the channel, so that the length of the channel (expressed in terms of the number of channel widths) required for complete mixing would be of the order of:

$$\frac{Z}{w} = \frac{U_0 w}{D} \simeq \frac{v_m L_0}{D_A} = Pe \quad (13)$$

This dimensionless number, known as the Péclet number, expresses the relative importance of Convection vs. Diffusion. In this example, the number of channel widths required for full mixing varies linearly with Pe . Using a standard Diffusivity for a small protein ($4 \cdot 10^{-7} \text{ cm}^2/\text{s}$) flowing with the fluid through a $100 \mu\text{m}$ channel at $100 \mu\text{m}/\text{s}$ requires $Pe \sim 250$ channel widths (approximately 2.5cm and 4min) to completely mix.

This particular device has been utilized as a sensor by exploiting the differences in Convection and Diffusion of different mixtures. T sensors have been used to measure analyte concentration [13] and analyte diffusivities and reaction kinetics [12,14]. Finally, competitive immunoassays have been performed by injecting an antibody solution alongside a solution of known, labelled antigen. Antigen-antibody binding is evidenced by marker accumulation in the interdiffusion zone, and an unmarked antigen can be detected differentially, as competition for antibody binding alters the marker profile measured downstream [15].

Another application based on a similar principle has been the ***H-filter*** (Figure 5).

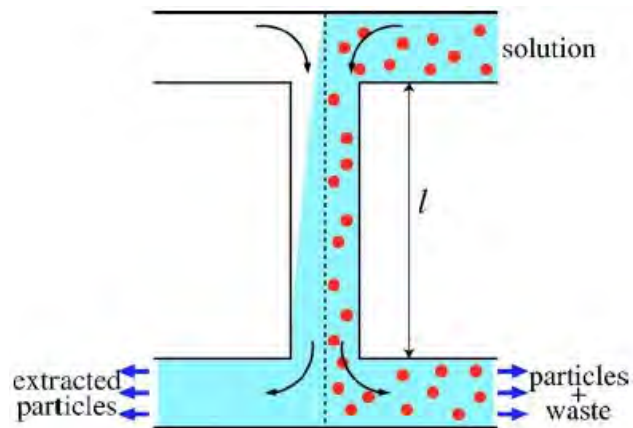


Figure 5: *H-filter*

This simple device filters particles by size without a membrane [16,17]. As in the T -sensor, two different streams are brought together to flow alongside each other down a channel. One stream is a diluted solution of different-sized molecules or particles, each of which has its own diffusivity and *Péclet* number. Using the simple argument above, each Pe determines the channel length required for that component to diffuse across the channel width. The *H-filter* works when the length l or flow velocity U_0 is chosen so that one Pe is small and the other is large. Low- Pe small solute particles diffuse to fill the channel before exiting, whereas high- Pe large particles

remain confined to their half of the channel. A reverse *T-sensor* then re-segregates the flow into two streams, of which one contains mostly small particles, and the other contains both species. The *H-filter* requires only that the components to be separated spread at different rates transverse to the flow, and works regardless of the cause of the difference in dispersivity.

Different modifications of the *H-filter* have been developed, where, for example, motile sperm are separated from nonmotile ones [18]. Rather than differing in diffusivity, motile sperm rapidly and randomly swim to fill the channel, as compared with nonmotile sperm, which spread via diffusion alone. Here as above, the species that spreads quickly is extracted. Another device [19] demonstrates the type of analysis that can be performed with these principles. An *H-filter* brings a stream of cells into contact with a chemical agent that lyses the cell membrane, allowing certain intracellular molecules to escape. One output of the *H-filter* contains both waste cells and intracellular molecules. The other contains mostly the molecules of interest, which are then brought to flow alongside a stream of detection molecules in a *T-sensor* to probe various properties, e.g., identification or concentration.

Another strategy to create *mixing* on the microscale is utilization of *Chaotic advection* [20]. When particles in a fluid move unsteadily and chaotically, some of the fluid's volume elements are stretched and folded², decreasing the pathway for Diffusion to occur and so enhancing mixing. Turbulent mixing works on this principle and although Stokes flows are inherently laminar, particles under this regime can move with chaotic path lines (*Chaotic advection*) that stretch and fold fluid elements in a way similar to that of turbulent flows, arising from the non-integrability of the

² A more detailed Mathematical description of stretching and folding processes can be found in [30]

advection equations (eq. (12)) and also the non-steady term ($\frac{\partial}{\partial t} \rho \mathbf{v}$) in Navier Stokes equation (equation (4)).

As an example of *Chaotic advection-based mixing* the *staggered herringbone mixer* is presented here. A continuous flow system in a channel can be Chaotically mixed by creating secondary rotating flows. In this mixer these secondary flows are achieved by patterning grooves in the channel walls [21,22] (Figure 6).

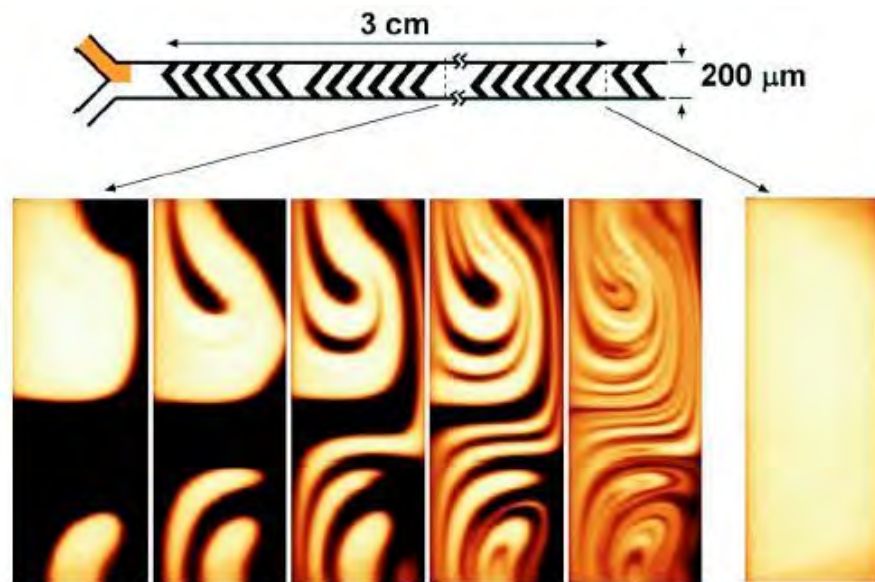


Figure 6: Staggered herringbone mixer

The asymmetry of the rolls is periodically reversed, so that the distance between stripes halves with each cycle, leading to exponential stretching and folding of fluid elements.

Although steady, incompressible two-dimensional flows cannot exhibit chaotic trajectories, steady three-dimensional and unsteady two-dimensional flows can have chaotic streamlines [20, 23]. As an example, oscillating flows driven across a main channel stretch and fold fluid in the primary flow onto itself, significantly enhancing mixing by reducing the pathlength for Diffusion [24].

In contrast to the Passive mixers described, the so-called *Active mixers* use external fields to generate disturbances that enhance *mixing*. Figure 7 shows different kinds of active mixers studied in the literature. They are all reported, with references, in the review paper [25]. The different external disturbances that have been applied and reported are Pressure field based (*a*, *b* and *c*), Electrohydrodynamic (*d*), Dielectrophoretic (*e*), Electrokinetic (*f* and *g*), Magneto hydrodynamic, Acoustic and Thermal.

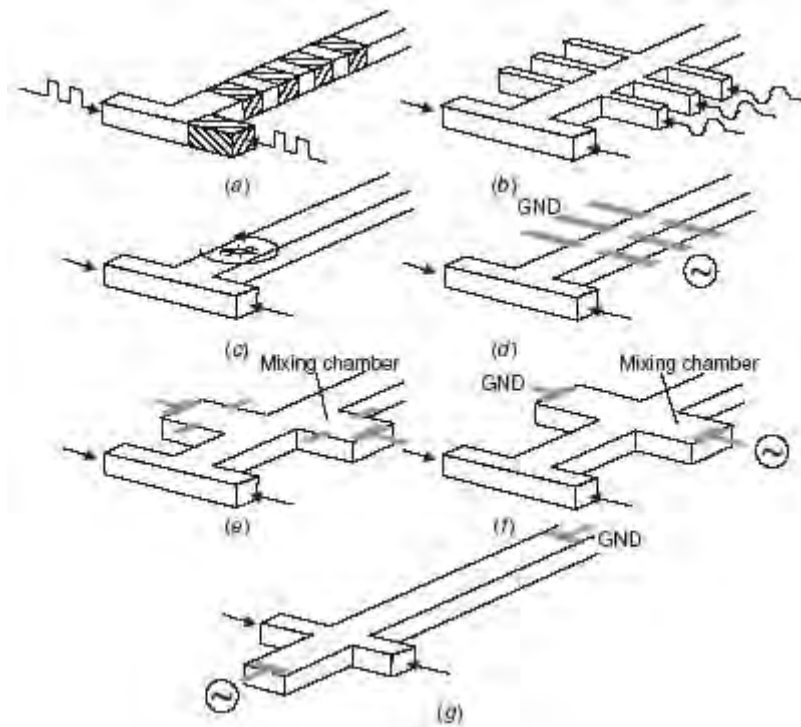


Figure 7: Examples of Active mixers

These mixers, as discussed previously, also rely on *Diffusion* and *Chaotic advection* for *mixing*, but the means by which this *Chaotic advection* is created are not passive, but active (externally generated).

2.4 Au/PPy Actuators

Conducting, or conjugated, polymers (CPs) are distinguished by *conjugation* (alternating single and double bonds between carbon atoms) along the polymer backbone. This conjugation results in a band gap, which makes the polymers semiconducting: when electrons are removed from these polymers (as when a sufficiently positive potential is applied) the charge on the polymer backbone becomes delocalized (because of the π electron system, called conjugation, the charge is easily shared among the backbone carbon atoms). This makes the CPs electrically conductive, in a very similar way as when Silicon is p-doped.

When a CP inside a solution becomes conductive, and so positively charged (oxidized), it will attract negatively charged ions so that electric neutrality in the medium is maintained. This process is called *doping*, because the attracted particles will usually penetrate into the CP matrix. The example of PolyPyrrole (PPy) is shown in the following Figure (Figure 8).

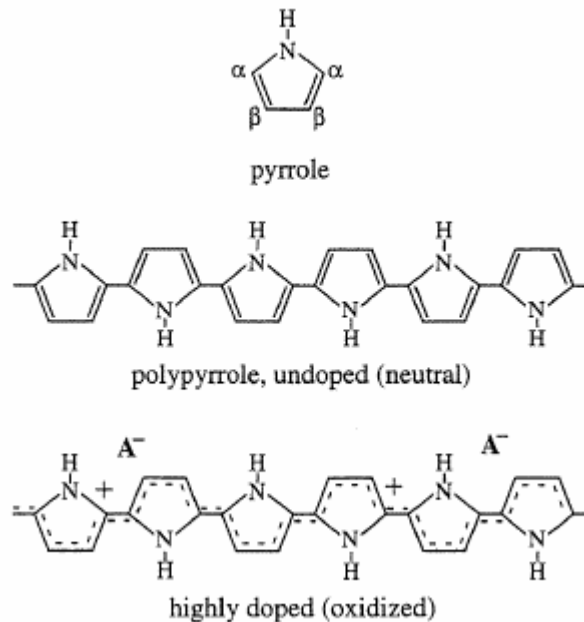
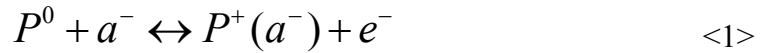


Figure 8: PPy backbone structure

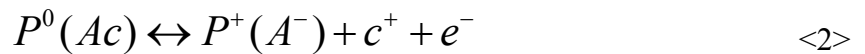
It is precisely this *doping* process (ion inclusion in the CP matrix) that makes CP attractive as actuators: the ion inclusion/exclusion processes are accompanied by an increase/shrinkage (respectively) of the CP volume [26].

CPs can be initially synthesized in either a neutral, or reduced, *undoped* state (without ion implantation) or a neutral *doped* state (with implantation of anions and cations).

Depending on the initial type of doping and the size of the ions used in this process, different reactions will take place during oxidation and reduction of the CP. If, like in the case presented in reaction <1>, there is no initial doping and the size of the anions in the solution is small (like Cl⁻) so that they can effectively penetrate the CP matrix, volume swelling will happen during oxidation, and shrinking during reduction.



If, like in reaction <2>, the CP is initially doped with a salt (like NaDBS) with big anions that will remain trapped in the CP matrix (dodecyl benzene sulfonate or DBS), and small cations that can penetrate the matrix (Na⁺), volume swelling will occur during reduction, and shrinking during oxidation.



As can be seen, many other configurations are also possible, but we will focus on a particular application of reaction <2>, where PPy acts as the CP and NaDBS, as the dopant [27].

The particular actuators that will be fabricated and tested in the context of this work will be the so-called Au/PPy actuators or “flaps” (Figure 9).

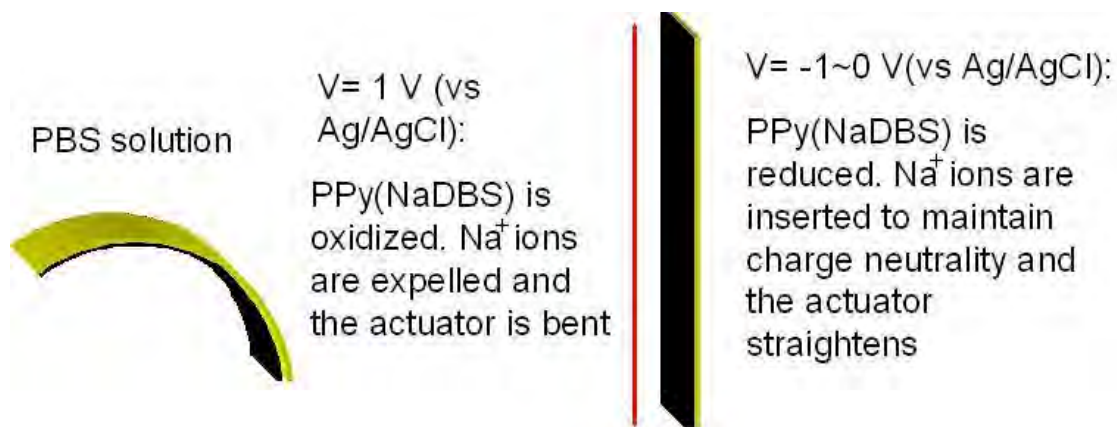


Figure 9: Au/PPy actuator

The bilayer structure of Au and PPy moves because the Au layer (whose volume is preserved) presents a constraint for the swelling/shrinkage of PPy. Thus the only possibility for the PPy to move is to bend upwards or downwards also forcing the deflection of the attached rigid layer (which is thin and very flexible due to the Au's low Young modulus). Without the Au layer constraining the PPy freedom of movement, the Polymer would swell and shrink in all directions equally, and much smaller amplitude of movement would be achieved.

Fabrication, Properties, and various applications envisioned for these actuators have been reported [26-29].

2.5 Electrochemical measurements

In this chapter a short review on the specific electrochemical methods that will be used within the scope of this work will be presented.

The main purpose of electrochemistry is to study the phenomena related to the transport of charge across the interface between different chemical phases, like an electronic conductor (electrode) and an ionic conductor (electrolytic solution).

Some chemical reactions (called Redox) involve the exchange of electrons between different species. When coupling these reactions with electronic circuits, capable of detecting electrical currents or providing electrical potential differences, a diversity of processes can take place that can be used in many applications: chemical detection, devices fabrication, corrosion protection, energy production, etc.

When an electrode is submerged in an electrolytic solution both *Nonfaradic* and *Faradic processes* can occur.

The most relevant *Nonfaradic* process is the formation of the so-called *electrical double layer*: at a given applied potential a charge is created at the electrode's surface (due to excess or deficiency of electrons) and a corresponding charge of the same magnitude and opposite sign is induced in the solution (due to an excess of either cations or anions in the vicinity of the electrode's surface). This system behaves like a Capacitor with capacitance C_d (which, unlike real Capacitors, is a function of the applied potential), and the solution acts like a resistor, R_s , so that the total system in the Figure 10 can be modeled as the electronic circuit:

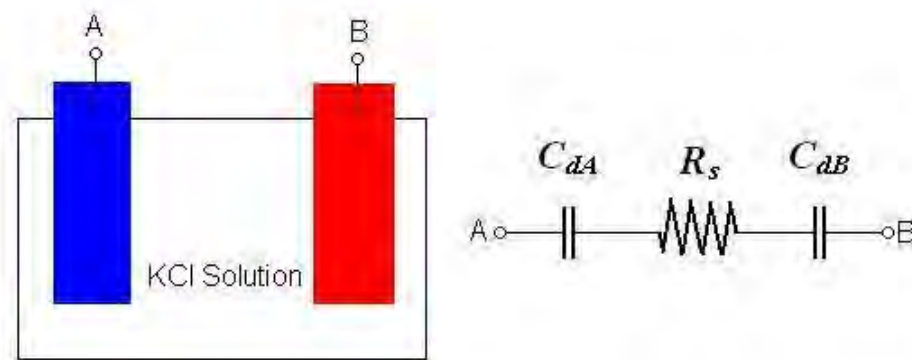


Figure 10: Electrical equivalent circuit to two electrodes in solution

If the electrode B (*Reference electrode*, RE) has a much bigger capacitance than electrode A, the total capacitance of the circuit would be:

$$C_{dT} = \frac{C_{dA}C_{dB}}{[C_{dA} + C_{dB}]} \approx C_{dA} \quad (14)$$

In this case, if the circuit is supplied with a Potential Source and an Amperometer (Figure 11)

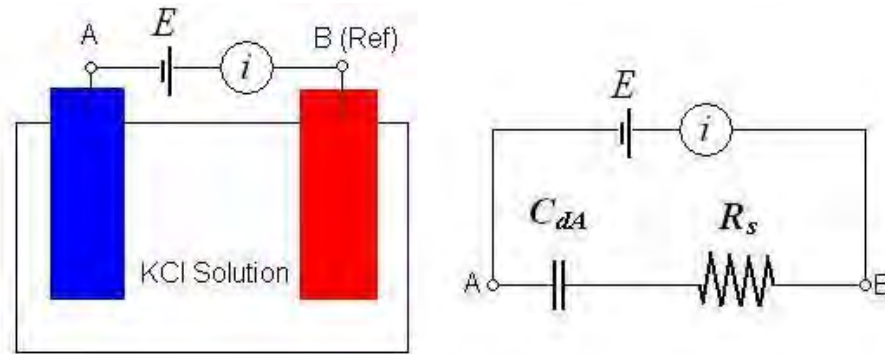


Figure 11: Potential source and Amperometer coupled with two electrodes in solution and equivalent circuit

the response of the current after an applied step Voltage (E) is presented in the Figure 12.

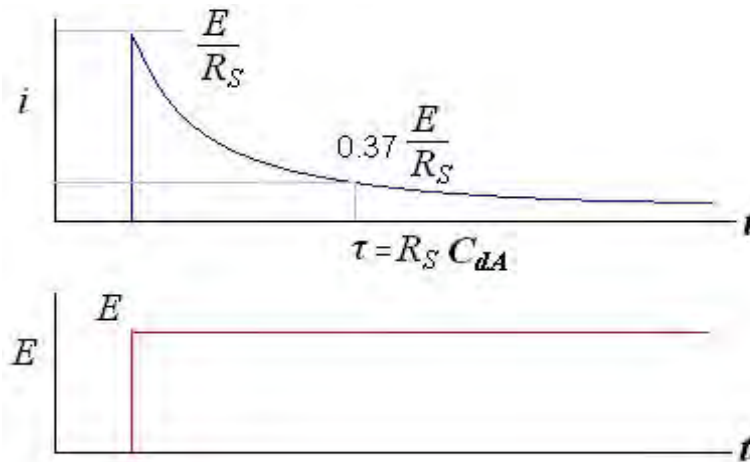


Figure 12: Nonfaradic current response after a Potential step experiment

The current will fall according to the equation:

$$i = \frac{E}{R_s} e^{-t/(R_s C_{dA})} \quad (15)$$

This transient current, i , is a result of the charging of the double layer “capacitance”, and has nothing to do with the chemical reactions that might be taking place at the electrode-solution interface.

Faradic processes occur when electrons are transferred across the metal-solution interface and reduction or oxidation reactions at the electrode-solution interface are taking place. An example of this could be the oxidation of a metal electrode, where a layer of oxide (*rust*) appears on the surface of a submerged metal as a result of an applied voltage. These reactions are governed by *Faraday’s law of electrolysis*, eq. (16), and they only occur when specific thermodynamic requirements are met (i.e. when a certain activation energy, in the form of an electric potential, is applied).

The rate of the Faradic process is expressed as:

$$Rate = J = \frac{i}{nFA} \left[\frac{mol}{m^2 \cdot s} \right] \quad (16)$$

where A is the electrode’s surface area, n is the stoichiometric factor for the electrons involved in the reaction, and F is Faraday’s constant ($9.64853 \cdot 10^4 C$).

Each system of electrode(s) and solution(s) has a particular minimum activation energy (also called “formal potential”, E^0) that is required for a given Redox reaction of certain species, with standard 1M concentration at 25°C, to take place. Some electrodes behave “indifferently” to applied potentials (RE), and they will neither promote any reactions nor interfere *Nonfaradically* with the system.

When a solution with a particular concentration, different than 1M, of certain species (let’s consider $Fe(CN)_6^{3-}$ and $Fe(CN)_6^{4-}$, at 3M and 1M respectively) is coupled with an electrode (Working electrode, *WE*) of such material (like *Au* or *Pt*)

that, under the range of potentials used it will not react with the solution, altogether with a reference electrode (RE), an *Equilibrium Potential (E)* is established between the RE and the WE. This *E* is the minimum energy (in Volts) that should be applied to the electrode for the reaction <3> to reach equilibrium, and so to have a net current of 0 Amp in the system (Figure 13).

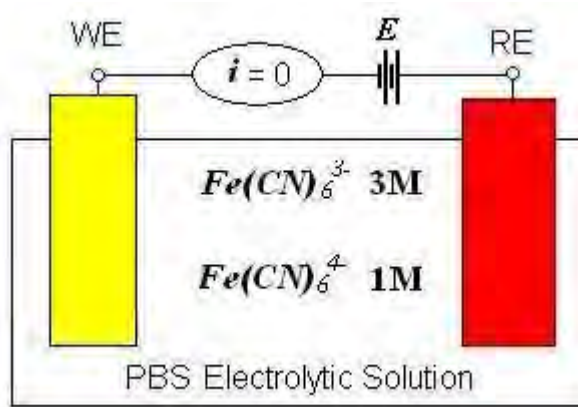


Figure 13: Equilibrium potential (*E*) definition

In this case, the Equilibrium Potential is determined by Nernst Eq. (17)

$$E = E^{0'} + \frac{RT}{nF} \ln \left[\frac{Fe(CN)_6^{3-}}{Fe(CN)_6^{4-}} \right] \quad (17)$$

If the applied potential (η , *overpotential*) is decreased with respect to the Equilibrium potential, the reaction will no longer be at equilibrium, and a reduction of the oxidized species will take place (Figure 14).

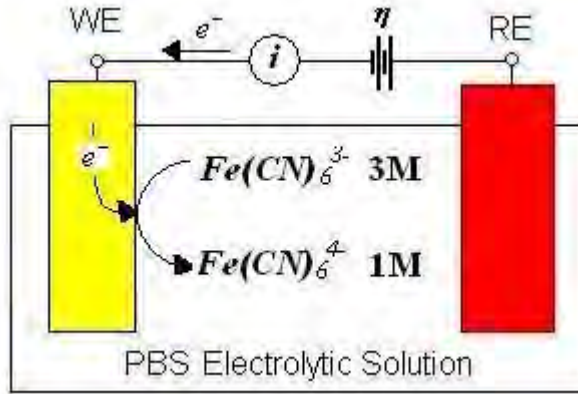


Figure 14: Reduction process when η is decreased with respect to E .

The presented example is a case of a *Faradic* process, in which, neglecting the mass transfer effects, the electronic current is proportional to the overpotential applied to the system, in the general form of the *Butler-Volmer equation* (18).

$$i = i_0 \left[e^{\frac{\alpha \eta F}{RT}} - e^{\frac{(1-\alpha) \eta F}{RT}} \right] \quad (18)$$

where i_0 is the *exchange current* (magnitude of the balanced anodic and cathodic currents associated with the equilibrium conditions) and α is the *transfer coefficient* (which is a measure of the symmetry of the energy barrier of the oxidized and reduced states, ranging from 0 to 1).

When mass transfer effects are also taken into account, the current, under some circumstances, is no longer a function of the overpotential alone. Assuming that the electrode kinetics at large overpotentials are sufficiently fast (which turns out to be the case for the $Fe(CN)_6^{3-/4-}$ couple) so that any species reaching the surface of the electrode will react immediately, the current can be limited by the mass transport rate at which these species reach the electrode's surface. This can be seen in the experiment presented in Figure 15.

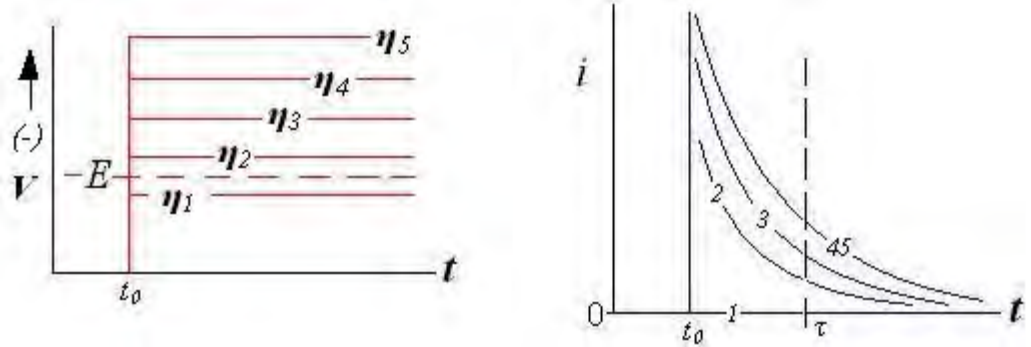


Figure 15: ChronoAmperometric experiments at different applied overpotentials

Different step overpotentials are applied at t_0 to a system, and the resulting current is measured over time (*ChronoAmperometry, ChA*). Initially, the concentration of the oxidized species at the surface of the electrode ($C_{O(0,0)}$) is equal to the bulk concentration (C_O^*). As soon as the overpotential is applied, though, the Oxidized species at the electrode surface are consumed and its concentration ($C_{O(0,t)}$) becomes 0. Thus, for the electrode reaction to continue, a sustained amount of Oxidized species has to be brought in contact with the electrode, and this can only be done by the different mass transport mechanisms presented in chapter 2.2.

If the applied overpotential is low enough, so that mass transport is faster than the electron transfer reaction (cases 1, 2 and 3 in Figure14), the current is reaction limited and so variations in the overpotential will lead to variations in the measured current. But, on the other hand, if the overpotential applied is high enough that the limiting process is the mass transport (cases 4 and 5 in Figure14), a situation is reached in which no matter how much the overpotential is increased, the effective current measured will be always the same (limited by the mass transport processes). This region of operation is called mass transport limited (Figure 16).

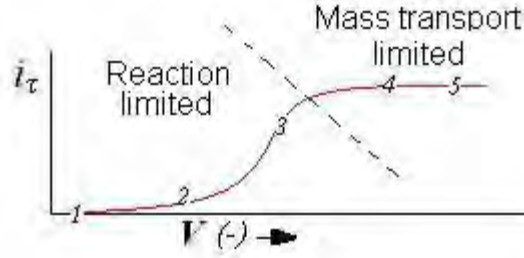


Figure 16: Construction of a Sampled current voltammetry or i - E curve

When operating at high enough overpotential so the system falls in the mass transport limited region, eqs (7) and (16) can be combined, so that the current is strictly a function of the mass transport phenomena:

$$i = nFA\mathbf{J}_A = nFA\left(-D_A\nabla C_A^* - \frac{z_A F}{RT}D_A C_A^* \nabla\phi + C_A^* \mathbf{v}\right) \quad (19)$$

When the reacting species are accompanied by other charged molecules at a higher concentration (like in Figure 13, where the medium is a Phosphate Buffer Saline), the migration term of the expression (19) can be neglected, so that only Diffusive and Convective transport affect the current:

$$i = nFA\mathbf{J}_A = nFA\left(-D_A\nabla C_A^* + C_A^* \mathbf{v}\right) \quad (20)$$

Under these circumstances, a simple electrochemical experiment (like ChA) can be used to determine different parameters of the system: the concentration of the species (when the Diffusivity and the velocity field are known), the Diffusion Coefficient (when the Concentration and the velocity field are known) or even the velocity field can be estimated (when the concentration and Diffusivity are known).

For the general case where $O + e^- \rightleftharpoons R$ the simplest ChA experiment is the one that relies on Diffusive mass transport only, and the expression for the resulting current has the form of the *Cottrell eq.* (21):

$$i_d(t) = \frac{nFAD_o^{1/2}C_o^*}{\pi^{1/2}t^{1/2}} \quad (21)$$

It must be noted that during a real ChA experiment, *Nonfaradic* effects will also take place (eq. (15)), so that they have to be subtracted from the actual reading of the Amperometer to obtain only *Faradic* current. For this purpose R_s and C_d must be calculated, which can be easily done with a control Blank ChA experiment in the same electrolytic solution without the Redox species (and so with only *Nonfaradic* effects present), as seen in Figure 11.

A ChA experiment can, then, be used to quantify the degree by which a micromixer, acting in combination with an electrochemical sensor, increases the diffusion-limited response of the sensor in the presence of a Redox reacting species. When the micromixer is not active, the current response of the sensor will be totally diffusion-limited, and will follow the form of eq. (20). When the micromixer is active, the response of the sensor will also be influenced by convective effects (such as *Chaotic advection* and convective reduction of the Diffusion Boundary layer as discussed in chapter 2.2 above).

ChA is also a simple experiment, reliable (electric current can be easily measured/monitored), and time-dependent (allowing for a time-evaluation of the micromixing process).

2.6 Electromagnetic interference

For interpretation of the collected results it is also important to discuss electromagnetic interference (EMI) and its mechanisms.

All electronic devices give off electromagnetic emissions. This is radiation that is a byproduct of electrical or magnetic activity. Unfortunately, the emissions from one device can interfere with work of other equipment located in the proximity of the emitting devices. This coupling effect is called EMI.

EMI can be caused by three main reasons: *Conductive*, *Capacitive* or *Inductive Coupling*. In the first case several electrical circuits share the same physical pathway, and they interfere with each other conductively. *Capacitive Coupling* happens when several electrical circuits have components in close proximity and at least one of them is under a time-varying electric field. Under these circumstances a Capacitance between the circuits is generated, which couples them as presented in Figure 17.

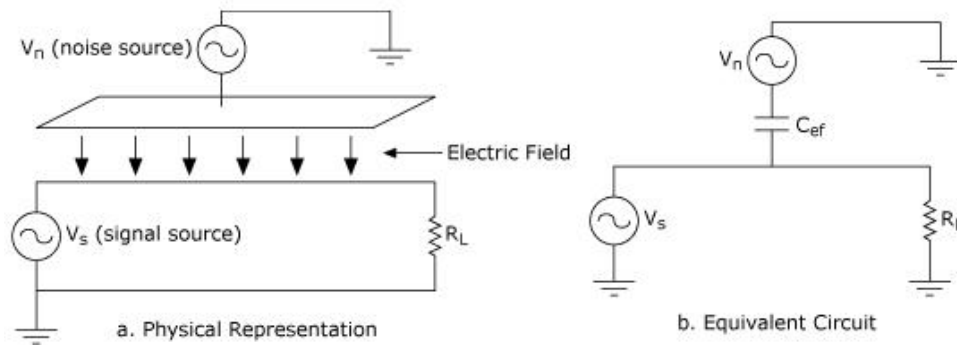


Figure 17: Example of Capacitive Coupling

Thus, when a current flows through the system under a time-varying electric field, a "noise" current is capacitively induced in the "signal" circuit.

Finally, the third source for EMI is *Inductive Coupling*. This occurs when a "noise" magnetic field (which can in turn be generated by a varying electric field of a "noise" circuit) is reaching a "signal" circuit. According to *Ampère-Maxwell's law*, a magnetic field can generate a current in a conductor as per eq. (22):

$$\nabla \times \mathbf{H} = \mathbf{J} + \frac{\partial \mathbf{D}}{\partial t} \quad (22)$$

where \mathbf{H} is the magnetic field, \mathbf{J} is the current density and \mathbf{D} is the electric displacement field.

An example of this is presented in Figure 18.

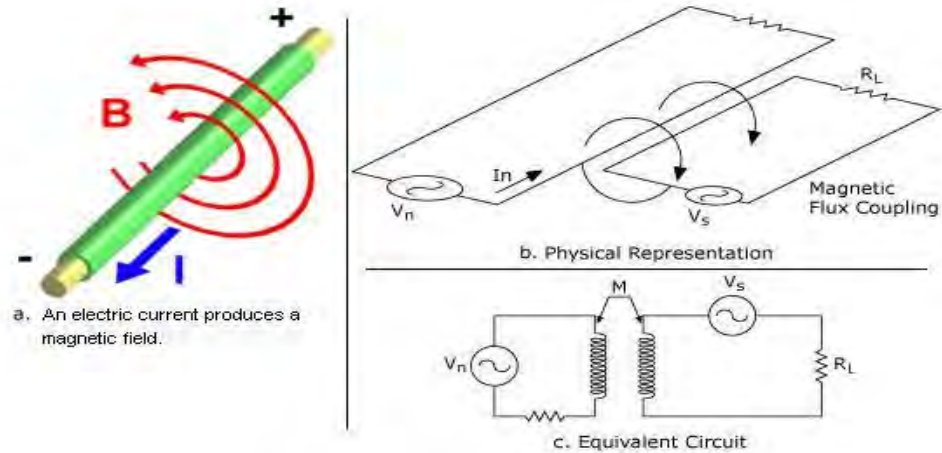


Figure 18: Example of Inductive Coupling

When experimenting with miniaturized electronic devices, the presented phenomena will have a big impact on any electrical signal measurements, mostly because the distances between interfering (“noise source”) and signal circuits are very small, usually microns in size. Therefore, it is important to keep in mind how these interferences behave, so a proper method for signal filtering and interpretation can be developed.

3 Objectives

The basic aim of this project was to test the feasibility of using Au/PPy actuators for active Micromixing. This goal was achieved by fabricating different Au/PPy actuator configurations and actuating them in the vicinity of a Redox sensor while performing a ChA experiment in the Diffusion-limited region of operation (as explained in section 2.5, Figure 16).

Three sensor-actuator systems, presented below, were explored: *Sensor near Flap*, *Sensor on Flap*, and *Micro Sensor near Flaps*.

3.1 Sensor near flap (*SnF*)

This set of experiments consisted of testing the ability of Au/PPy actuators, several mm in size, of increasing the response of a Au sensor placed right in front of the actuator, like depicted in Figure 19.

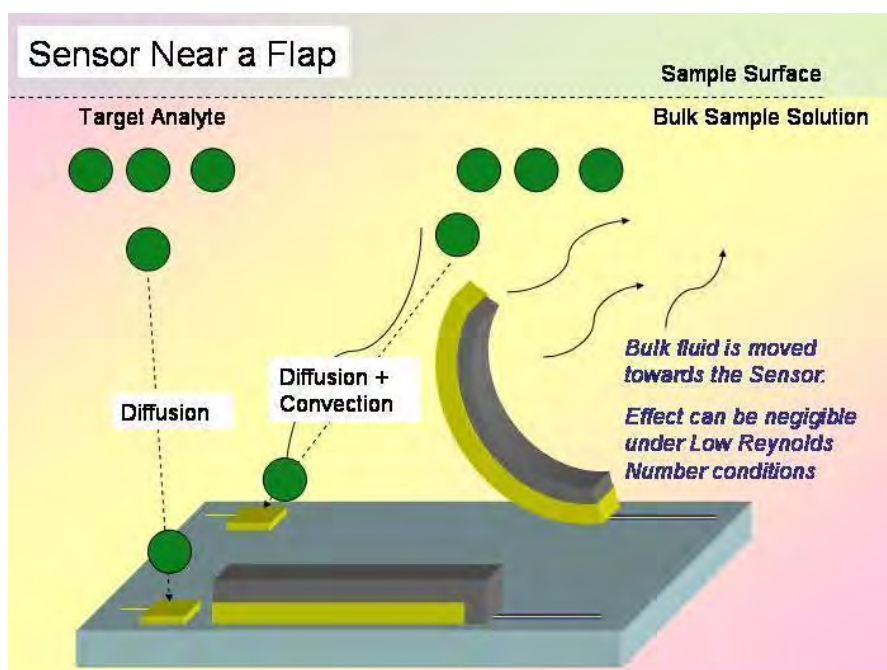


Figure 19: Sensor near Flap configuration

When the initial ChA experiment was run on the Sensor, a Diffusion-limited response was obtained. Once this Diffusive response was recorded, the actuator was activated in a new ChA experiment, and the new response incorporated (when cleared from interferences) the additional effects of any increased mass transport due to the particularities of the flow promoted by the working actuator.

The dimensions of the devices to be fabricated were envisioned as the ones presented, in mm, in Figure 20.

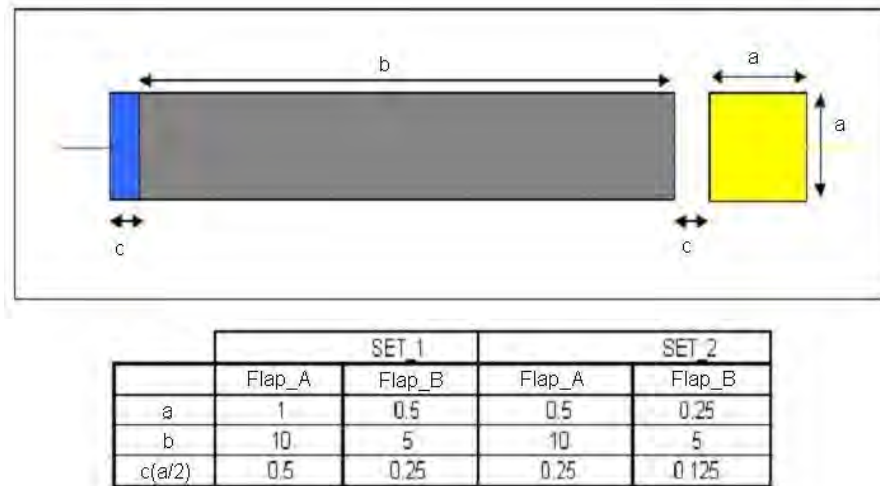


Figure 20: Dimensions of SnF fabricated devices

3.2 Sensor on flap (SoF)

This set of experiments was aimed at the fabrication and testing of a new sensor/actuator configuration. In this case, the goal was to place the sensor on the same actuator (as shown in Figure 21), so that ideally the sensor would be brought into the bulk of the solution, and perhaps this way an increased response (not only due to the flow of fluid, but also because the sensor itself is brought into regions of higher concentration) would be obtained when compared with the previous configuration.

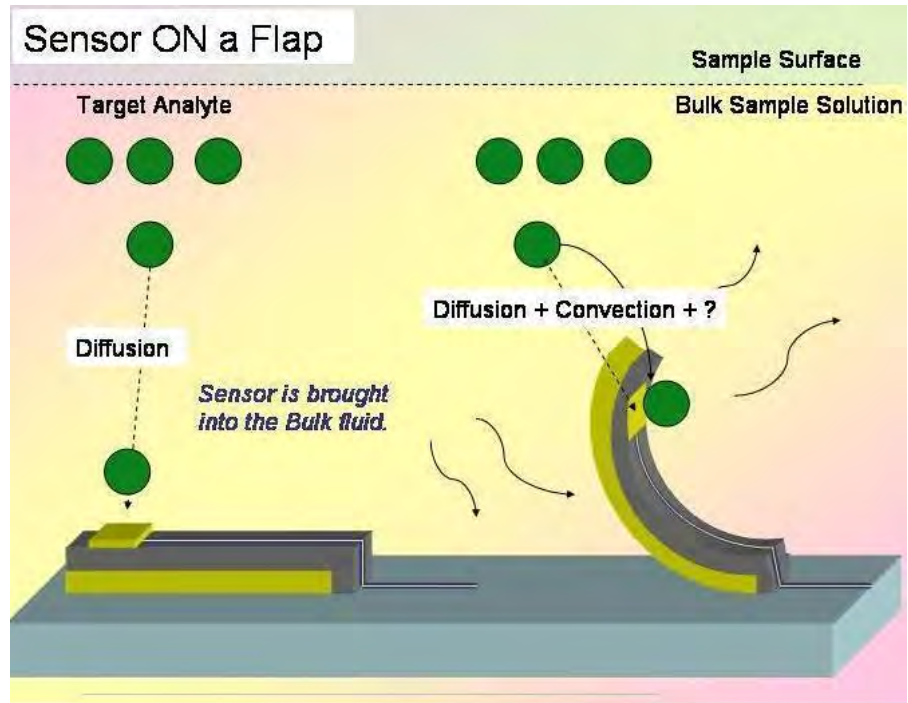
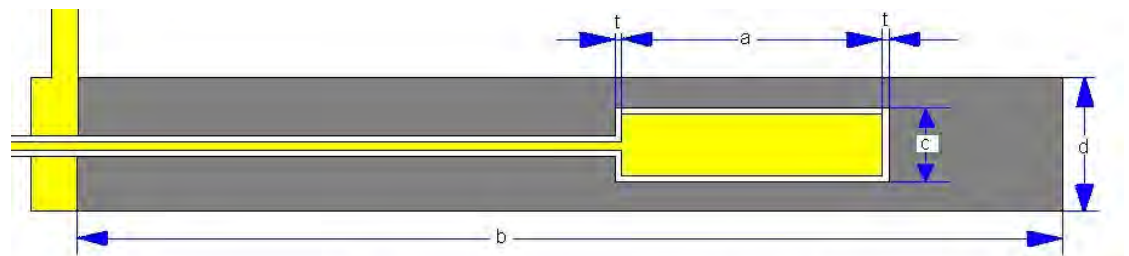


Figure 21: Sensor on Flap Configuration

The dimensions, again in mm, of this new set of devices are presented in the figure below (Figure 22).



	SET 1		SET 2	
	Flap_A	Flap_B	Flap_A	Flap_B
a	1	2	1	2
b	5	10	5	10
c	0.25	0.5	0.105	0.23
d	0.5	1	0.25	0.5
t	0.025	0.025	0.025	0.025

Figure 22: Dimensions of SoF fabricated devices

In this case, to avoid *Conductive coupling* between the sensor and the electrically activated actuator, an electronically insulating layer between sensor and actuator was needed.

3.3 Micro Sensor near flaps (*mSnF*)

Once the experiments described above were performed, and collected data was analyzed, we could take advantage of the conclusions reached from these experiments that employed large size actuators (which are easier to manufacture and observe) to plan a new set of experiments, this time with the goal of testing the effect of actuating several flaps, microns in size, to try to create *Micromixing*.

As discussed in the previous chapter, in the microscale domain low Reynolds numbers are predominant. This hinders the possibility to effectively create flows that would enhance mass transport (like turbulent flow). But nevertheless, as presented in Figure 1, it is possible for microsystems with more than two degrees of freedom to move (or “swim”) in these domains. If the particular system, like with Au/PPy actuators, is attached to a motionless substrate, what will actually move is the fluid around the system when the actuators (like the two hinges in the example of Figure 1) are activated. Thus, if a flow of certain characteristics could be promoted, effects like *Diffusion-Boundary layer* thickness reduction and *Chaotic advection* could take place to increase *mixing*.

For this reason, the next set of experiments employed a variety of actuators, with the aim of enhancing the previous effects and so effectively promote *Micromixing*, and thus enhance mass transport compared with what otherwise would be a diffusion-limited process.

The configurations tested are presented in Figure 23 below. The flap dimensions were 380 μm in length and 38 μm in width. The sensor was an octagon with side length of 38 μm . The distance between each flap and the near edge of the octagonal sensor

was $20\mu\text{m}$. 4 different configurations were designed: two configurations incorporated 2 actuators each and two other configurations incorporated 6 actuators each. In the first case the 2 actuators could be either actuated on phase by sharing the same connection line (*2 Flaps On-phase*) or they could be actuated 180° out of phase by connecting the “+” signal output of the Function Generator to one of them and the “-” output to the other (*1vs1 Flap*).

In the second case, with 6 actuators, the same principle was applied: the first set consisted of 6 actuators activated on phase (*6 Flaps On-phase*) and the second set consisted of 3 actuators moving 180° out of phase with respect to the other 3 actuators (*3vs3 Flaps*).

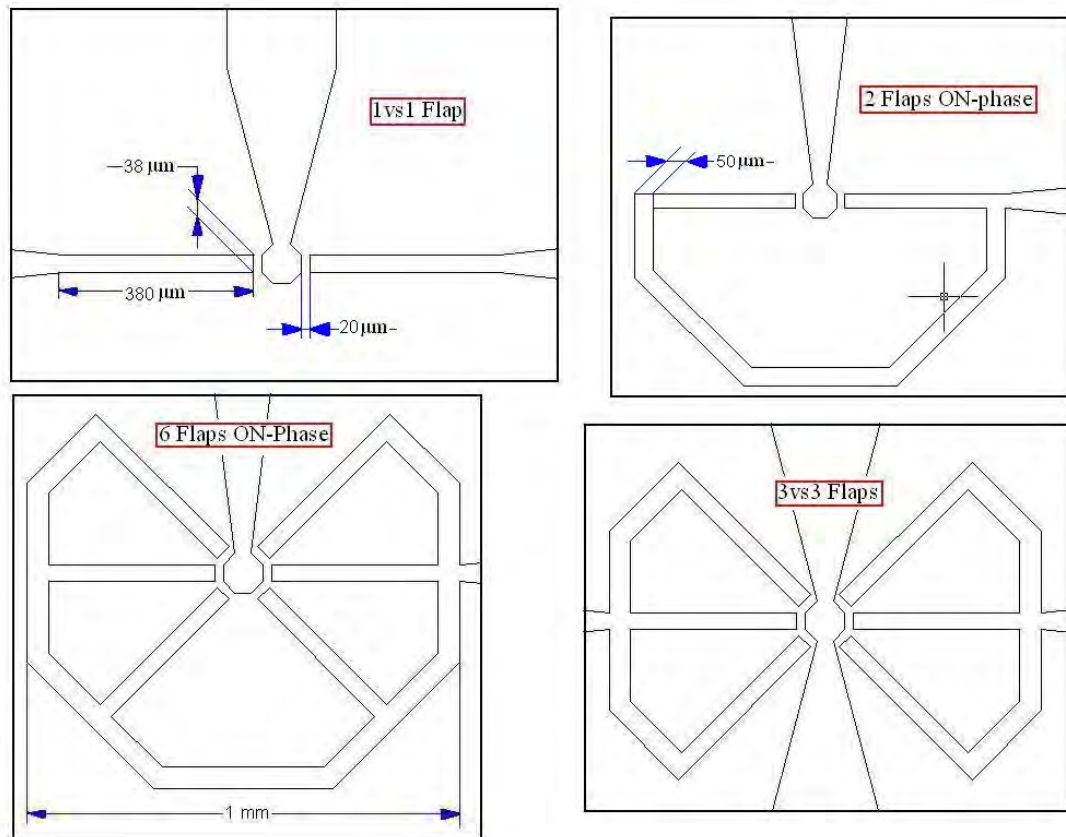


Figure 23: Configurations and Dimensions of *mSnF* fabricated devices

4 Experimental Work

4.1 Device Fabrication

All devices were fabricated at the Integrated Nano Research Facility at UCI. The fabrication process for the *SnF* and for the *mSnF* (Figure 24) are different from the fabrication process for the *SoF* (Figure 25).

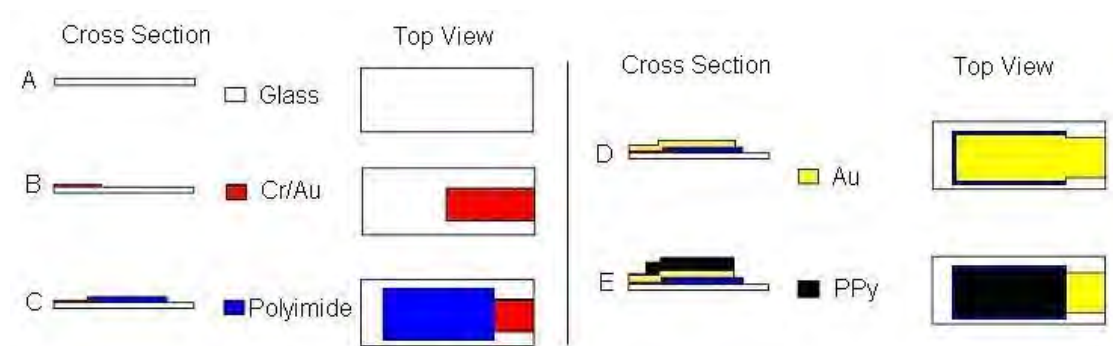


Figure 24: Fabrication process for *SnF* and *mSnF*

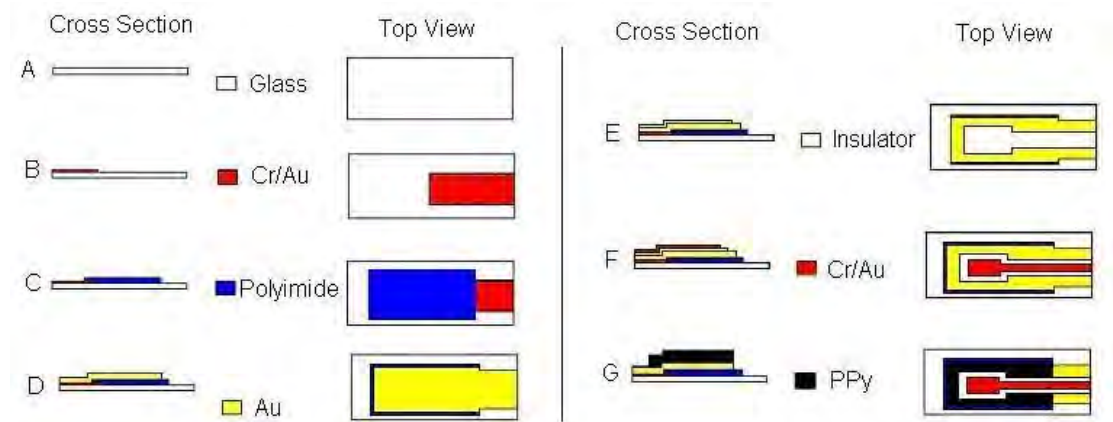


Figure 25: Fabrication process for *SoF*

In the following subsections a brief description on each process flow is given.

4.1.1 Masks Fabrication

All masks were designed with AutoCad2000, and sent for printing to “Photoplot store” (<http://www.photoplotstore.com/>). The dimensions of the designed devices were the same as presented in Figures 20, 22 and 23.

Once the ink-patterned films were received and prepared, they were transferred to a 5” Iron Oxide (FeO) mask: the films were placed onto the Photoresist (PR) covered face of the FeO masks and exposed with UV light (exposure time depending on UV-light power). Then the PR was developed, revealing the FeO layer. This layer was removed with FeO etchant (etch time was gauged by observing if FeO layer was still visible). Finally the Mask was stripped of PR with acetone and DI water, and the final FeO patten was revealed.

4.1.2 Sensor near flap (SnF)

As indicated in Figure 24, *step A*, initially glass slides were cleaned with DI water, acetone, and isopropanol. After that, the samples were introduced into a thermal e-beam evaporator metal deposition system, where first a thin layer of Chromium (Cr), between 30 to 80nm, and then a Gold (Au) layer, ranging from 25 to 100nm were deposited onto the exposed faces of the glass samples.

Shpiley 1827 PR was then spin coated on the Cr/Au deposited surface, at 3000rpm for 30s. After a 2min soft-bake at 90°C (either in furnace or hot-plate) the sample was exposed under the appropriate FeO mask. Then the Cr/Au patterns to be etched were revealed by developing the exposed PR. After this, first Au etchant and then Cr etchant (for as long as required) were used to etch away the undesired metal

coverage, so the Cr/Au was only present on the desired areas of the substrate, which would be used as “Electrical contact pads and lines” (*step B*).

Then a thin layer (ranging from 100nm to 500nm, depending on the spin coating time and velocity) of diluted PIRL-III, a Polyimide containing solution, was deposited, soft-baked (at 200°C for 10 min) and patterned. Polyimide patterning was done by depositing a PR layer on top of the Polyimide, exposing it under the appropriate mask and developing it very carefully, because Polyimide is also dissolved by positive photoresist developers, and depending on the deposition process and bake temperature, it can be deeply “*undercut*” from below the PR (as in Figure 26). Once patterned, the PR was stripped with acetone and the final Polyimide pattern was obtained (*Step C*).

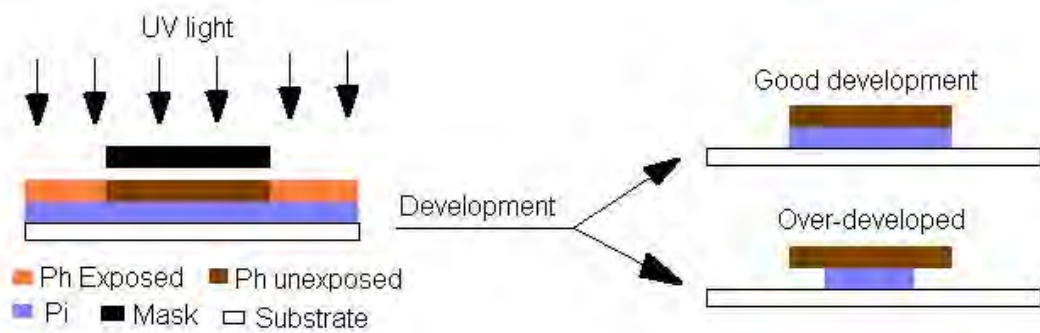


Figure 26: Undercut effect on Polyimide when developing PR.

This Polyimide layer is often called *addition layer*, and it's only necessary when the future Au layer of the flap adheres strongly to the underlying substrate and they are difficult to separate once put in contact. We manufacture PPy/Au on glass, and in this case PPy/Au have usually better mutual adhesion properties than Au/glass: Also when the devices are small (PPy actuation force scales up at smaller dimensions) an addition layer is often not required. Nevertheless it is convenient to add a Polyimide layer in

between Au and glass, because the Au/Polyimide adhesion is very weak, and this way a faster detachment with less power requirement is achieved.

When the Polyimide layer was patterned, the thermal e-beam deposition of the final Au layer of the flap was performed. This time the thickness of the Au layer was always 300nm. Again, PR patterning was performed, and the undesired Au areas were etched out. Remaining PR was stripped and the final Au layer of the flap was exposed (*Step D*).

The final process was the PPy deposition. For that purpose a solution of 0.1M Pyrrole and 0.1M NaDBS was prepared. The microfabricated device was introduced in the solution and connected (via the initially patterned connection pads) to the WE of a Potentiostat³. A RE (trying to maintain its tip as close as possible to the Au area to be deposited on) and a Au *Counter Electrode* (CE), with large area, were also submerged in the solution and connected to the Potentiostat. Then a ChA experiment was run at 0.6V for as long as required (depending on the area of the Au layer on which PPy was being deposited) to deposit a 3 μ m thick layer of PPy⁴.

4.1.3 *Sensor on flap (SoF)*

In this case the fabrication process was the same as the previous one, but with added steps (Figure 25).

³ Gamry Femotstat FAS2

⁴ PPy Thickness measurement was done on Tencor Alpha-Step 200 Surface Profilometer

After the Au layer of the flap was patterned (*Step D*), an insulating layer had to be deposited on it to avoid electrical contact between the future sensor and the flap. This layer was mainly fabricated with two different materials; SU-8 PR and Polyimide, with various thicknesses, ranging from 1 to 20 μm . Depending on whether the insulating layer was patterned with SU-8 or Polyimide, different fabrication processes and masks were used, with the final result as presented in Figure 25, *Step E*.

After this, the Sensor was to be placed on the insulating layer. This was done by a thermal e-beam deposition of a first layer of Ti (from 50 to 80nm thick) and a second layer of Au (from 50 to 80nm thick). PR was then exposed and developed so that the Ti and Au layers could be afterwards etched away from the undesired areas. Note that when Au is first etched, Ti behaves as a protective layer that covers the initial Au layer of the flap, and so only the later Au layer of the sensor is patterned. When Ti is etched, the previous Au and Cr layers appear, as in *Step F*.

Finally PPy was deposited as mentioned in the previous case, *Step G*.

4.1.4 *Micro Sensor near flaps (mSnF)*

This process was exactly the same as described in 4.1.2 with the exception that thicknesses of the material layers were different from the *SnF*.

In *Step C*, the Polyimide layer was made as thin as possible, in order to maintain the continuity of the contacts with the Au layer of the flap. Layers ranging from 50nm to 200nm thick were deposited (at spin coating speeds ranging from 3000 to 7000rpm for 30 to 70s). Different bakes (ranging from 200 to 300°C for as long as 2h) were performed on the Polyimide trying to reduce the undesired undercut effects (Figure

26) during PR development. PR development time and agitation were also optimized, so that finally a good Polyimide shape with minimum thickness was obtained.

Several different samples with Au layer thicknesses of the flap ranging from 30 to 300nm were also fabricated, *Step D*.

Finally, PPy was deposited (*Step E*). The PPy layer thickness was kept in 10:1 ratio with respect to the total Au layer thickness as suggested in the literature [25].

4.2 Flaps Actuation

All flaps were actuated in a Phosphate Buffer Saline solution (PBS: 137mM NaCl, 10mM Phosphate and 2.7mM KCl. PH 7.4). The actuation source was an HP/Agilent 8116A Function Generator (FG), and the functions applied were sinusoidal waves with amplitudes ranging from 0 to 2V and frequencies extending from 1 to 11Hz.

The “+” voltage output of the Function Generator was connected to the Flap(s). In the case of *mSnF* opposing phase configurations (*1vs1* and *3vs3* Flaps), the “-“ output was also used and connected to the opposing Flaps.

4.3 Electrochemical experiments

Several Electrochemical experiments were performed to test the ability of the fabricated devices to create Mixing.

Mostly only ChA experiments were run (although for characterization purposes some Cyclic Voltammeteries were also run), using $K_4Fe(CN)_6$ at different initial bulk

concentrations, C^* . A scheme of the setup used in all the experiments is presented in Figure 27.

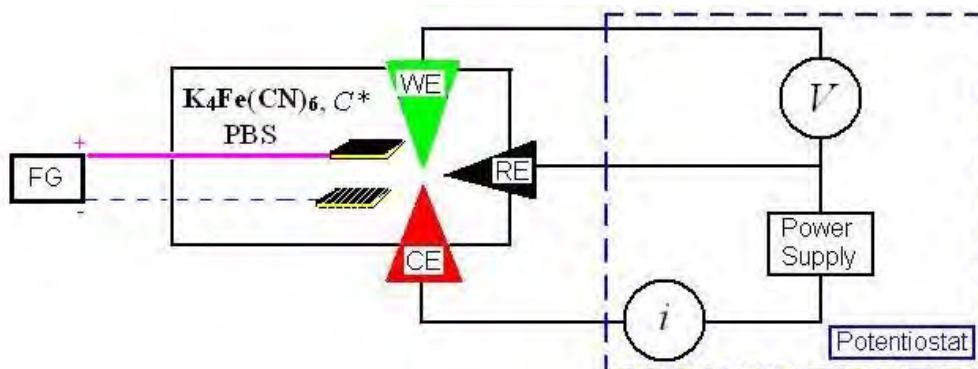


Figure 27: Scheme of the electrochemical and flap-actuation experimental set-up

The Potentiostat used was a *Gamry FAS2 Femtostat*. The WE was the Sensor (in *Near* and *On* the flap configuration), which was deposited by thermal e-beam evaporation by subsequently depositing Cr (to promote adhesion to the substrate - either glass, Pi, or SU-8) and Au (noble, chemically inactive metal in the range of potentials used in the ChA experiments) metal layers. The RE was an Aldrich Glass reference electrode (Calomel type). The CE was created by using a large surface area of Cr/Au bilayer deposited on glass.

The various experiments performed are presented in the sections below.

4.3.1 Current-Potential (i - E) Experiments

This set of experiments was carried out in order to determine the $\text{Fe}(\text{CN})_6^{4-}$ ion electron transfer reaction kinetics and so to find out the Reaction-limited and Mass transport-limited conditions (as in Figure 16) for this species in PBS electrolyte.

For different initial concentrations of $\text{Fe}(\text{CN})_6^{4-}$, C^* ranging from 0.1M to 10^{-5}M , a current-potential curve (like in Figure 16) at different ChA times (τ ranging from 5 to 25s) was constructed.

4.3.2 ChronoAmperometric Experiments

Two types of ChA experiments were run for every sample of each of the three (*SnF*, *SoF* and *mSnF*) different types of devices: **Diffusion-limited blank** experiments and **Mixing** experiments.

In the *Diffusion-limited blank* experiments, the ChA experiments were run on the sensor, with different initial $\text{Fe}(\text{CN})_6^{4-}$ concentrations (from 0.1M to 10^{-3}M). No $\text{Fe}(\text{CN})_6^{3-}$ was initially present (although it is conceivable that some amount was produced during initial experiments and so a trace concentration would be present in the final experiments). Thus, the Diffusion-limited response of the sensor was recorded (an example is given in Figure 28).

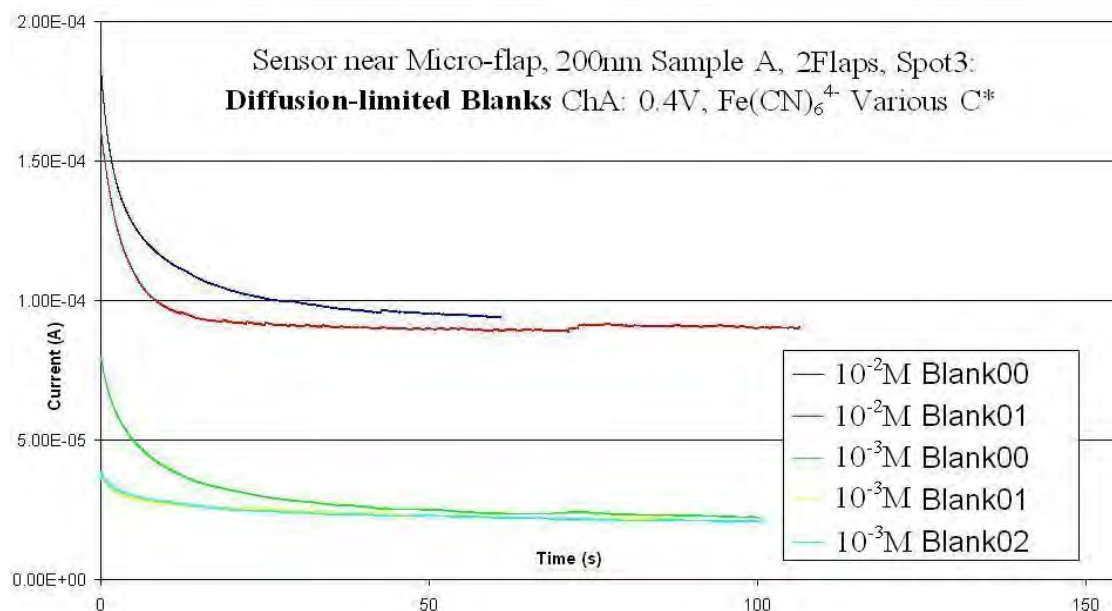


Figure 28: Typical Diffusion-limited response of several ChA experiments

For the *Mixing* experiments, the same ChA test was run, but this time the flaps were actuated. All data was video-taped, including the real-time movement of the flaps and the Amplitude/Frequency of the applied sinusoidal functions.

4.3.3 *Interference analysis and data filtering method*

During the *Mixing* experiments, it was clear that a strong EMI was induced on the sensor from the electrically driven flaps.

It is conceivable that Chemically-induced Interferences, due to Redox reactions promoted by the electrically charged flap, could also take place: the real bulk concentration, C^* , of $\text{Fe}(\text{CN})_6^{4-}$ in the vicinity of the sensor could be changed over time due to reduction/oxidation of the $\text{Fe}(\text{CN})_6^{3-/4-}$ couple on the electrically charged flap, which could behave as a Working Electrode in the solution. Therefore, when a ChA experiment was run, if the C^* was changing over time, the observed ChA current would be changing proportionally.

During the initial experiments it was observed that these interferences were clearly coupled with the applied function on the flaps (when a sinusoidal function was applied, a sinusoidal ChA response on the sensor was observed). A method was developed to filter the intrinsic response of the sensor (due to mass transport effects) from the influence of the electroactive flaps (that create EMI and concentration gradients that interfere with the sensor response).

For this purpose a third set of experiments, *Noise Blank* experiments, were run for each device configuration. They were like the previous ChA *Mixing* experiments with the difference that this time the Au/PPy flaps were substituted by the flap's Au

substrate layer without deposited PPy, which behaved as a motionless interfering electrode of *almost* the same dimensions (except for smaller thickness) as the working flaps. Thus the interfering phenomena was recorded and studied on a Diffusion mass transport-limited case (no Mixing due to flap actuation).

The goal of this new set of experiments was to test the nature of the interfering phenomena under Diffusion-limited circumstances. If the interferences were to be additive (“building up” on the underlying Diffusion-limited signal) they could be filtered by a simple numerical method capable of removing periodical effects (as shown in Figure 29).

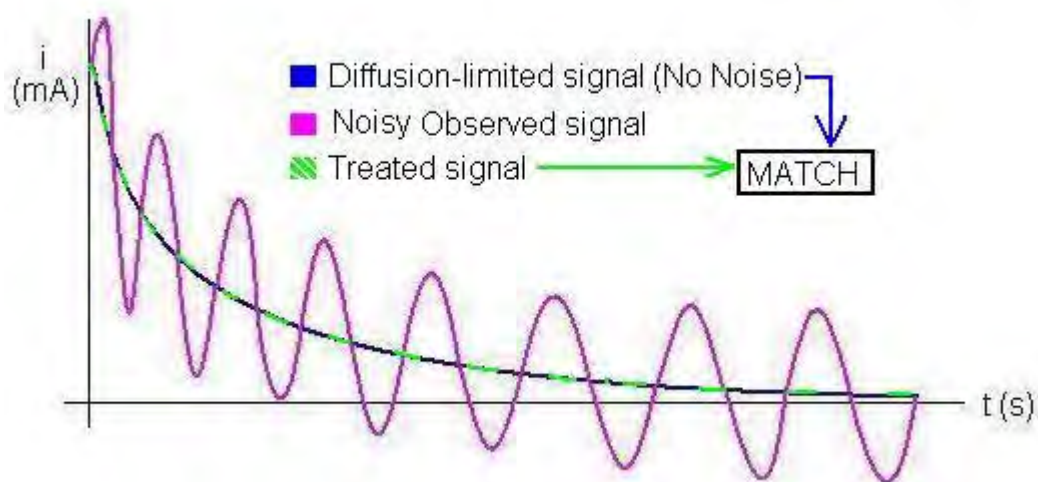


Figure 29: Ideal behaviour of the EMI and Redox interferences, which could be filtered by a numerical method capable of removing periodical components

Similarly, the same technique could be used to clean the results of the *Mixing* experiments. Comparison of the results of the “*clean*” *Mixing* experiments and the *Diffusion-limited Blank* experiments would give a final answer on the ability of the fabricated microactuators to improve mass transport by enhancing *mixing* (increasing what otherwise would be a Diffusion-limited process).

The numerical method developed to eliminate the induced periodic perturbations that obscure the intrinsic signal is presented here. The ChA response from the *Noise Blank* experiments was a *current vs time* data series that, depending on the time-scale of the experiment and the frequency of data acquisition (usually 0.01s), typically had 30,000 points. To effectively remove periodic components from the underlying signal, a set of new series was iteratively created. Each point of the new series was created by taking the average of 11 points of the previous series. These 11 points consisted of: 5 points that immediately preceded the data point of interest, the data point itself, and 5 points that immediately followed the considered data point. By iteratively repeating this process (typically 200 iterations) a final series was obtained, where the periodic components of the initial series were no longer present. This method is illustrated in the following Figure.

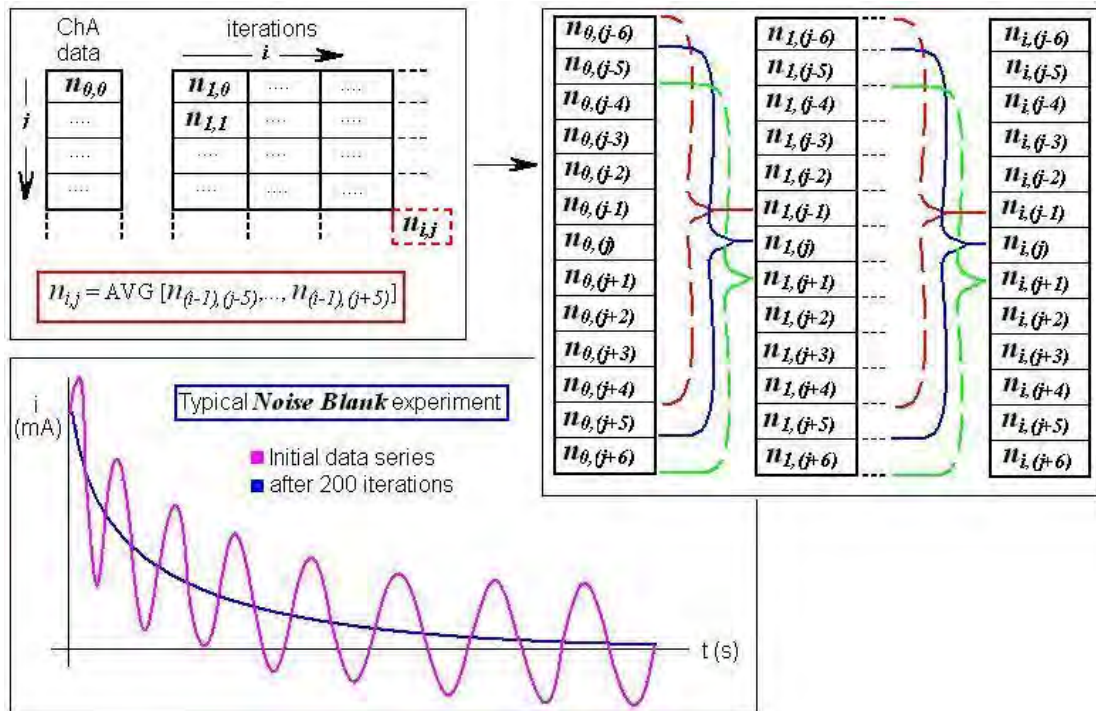


Figure 30: Numerical method for removal of periodic perturbations on an underlying signal

Figure 30 shows an example of a typical *Noise Blank* experiment, where an induced sinusoidal signal (purple) is building up on the underlying intrinsic signal (blue). This intrinsic response is only clearly observable after the numerical method is applied to remove the periodic interference.

The proposed numerical methodology would be enacted after verification that the results of the *Noise Blank* experiments treated with the numerical method presented had matched the results of the *Diffusion-limited Blank* experiments.

4.4 Flap Movement visualization and recording

For the *SnF* and *SoF* experiments, where the flaps were sufficiently large to be visible to the naked eye, a digital video camera was used, directly recording through the beaker containing the solution.

For the *mSnF* experiments, where flaps of micron size were actuated, a probe-station incorporating a microscope and a video capture system was used. The set-up is presented in Figure 31.

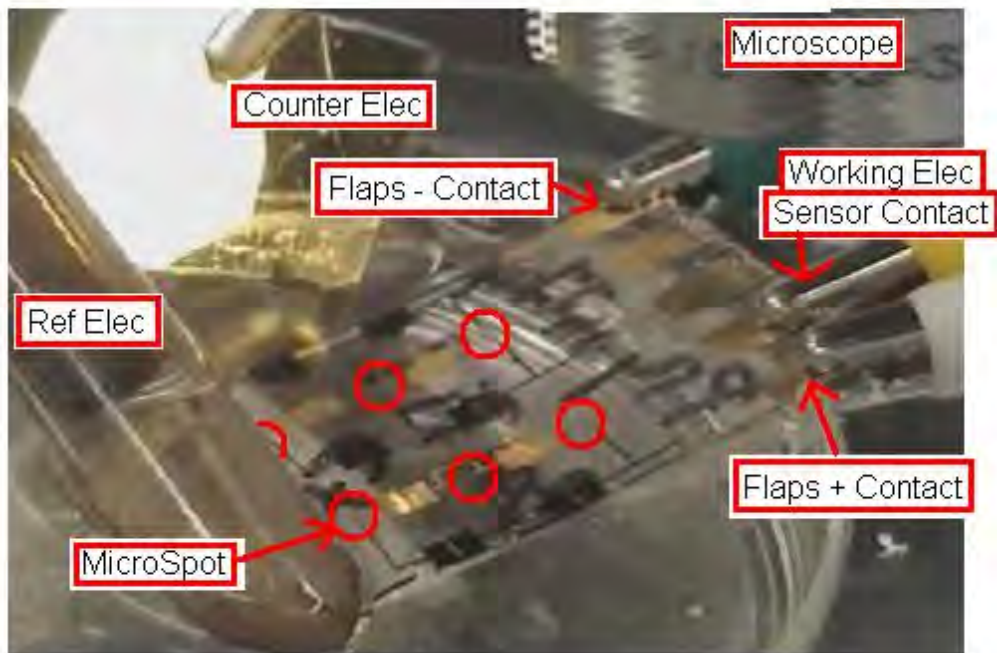
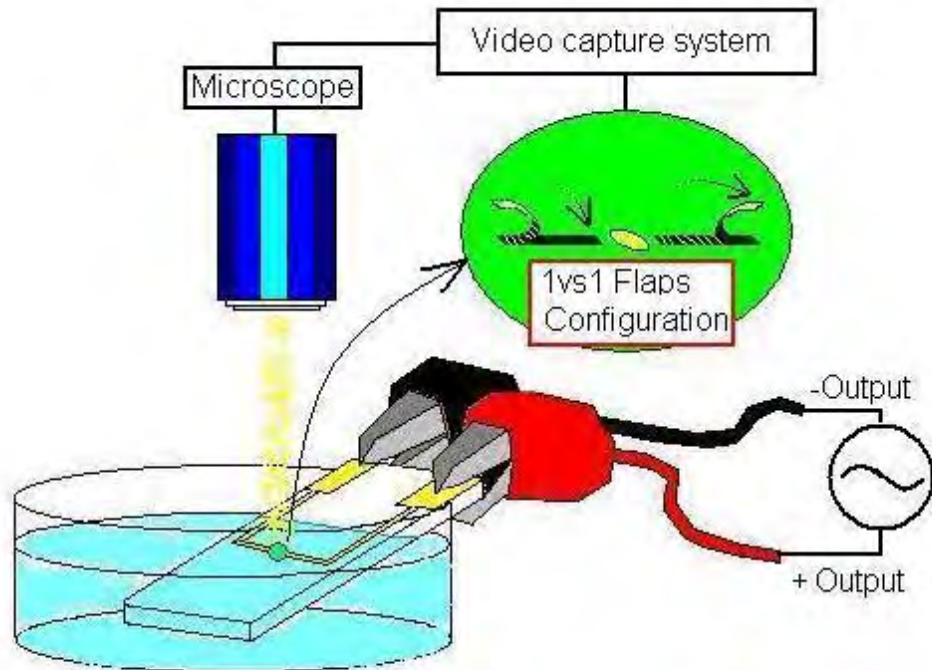


Figure 31: Set-up for the mSnF experiments

5 Results and Discussion

In this section the most relevant results on the different experiments performed will be presented and discussed.

5.1 Fabrication results

5.1.1 *Sensor near Flap (SnF)*

Some finished devices can be seen in Figure 32.

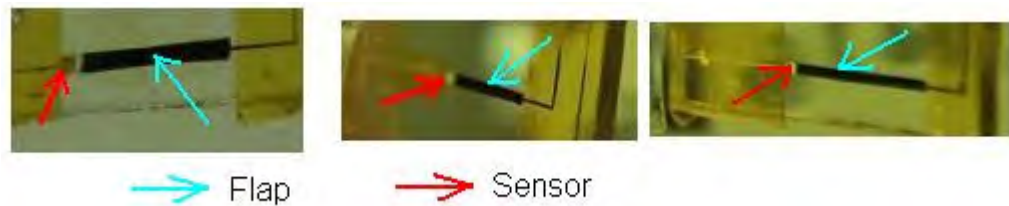


Figure 32: *SnF* devices

The PPy deposition method for these devices resulted in PPy layers 3 to 5 μ m thick which generally proved to work in a satisfactory manner (see section 5.2.5).

5.1.2 *Sensor on Flap (SoF)*

In this case the fabrication of the devices was considerably more complicated than in the previous case, because in order to achieve a device that could be successfully tested, the following conditions had to be met:

- a. The final flap should retain maximum flexibility even with the added insulating layer, so that a “normal actuation” (similar to the *SnF* devices that do not incorporate such insulating layer) could be reached.

b. The sensor should be perfectly electronically-insulated from the actuator. This means that none of the parts of conducting elements (Au, Cr, and PPy on the flap, and Au and Ti on the sensor) could be in contact. This was essential to avoid any further interferences (*Conductive coupling*) on the reading of the sensor.

The most critical part of this fabrication process was to find an optimum trade-off between electrical insulation quality (directly proportional to the thickness of the insulating layer) and retention of flexibility (which is inversely proportional to the insulating layer thickness).

In the process of finding the optimal thickness of the insulation layer that will ensure good actuation properties, another process issue came to our attention: 3-D nature of the electrochemical PPy growth. In some situations when thin insulation was sufficient to provide electrical insulation while maintaining the required flexibility, the lateral growth of PPy would create a short circuit.

The initial fabricated devices didn't take this fact into account, and so thick insulating layers were needed for good insulation (Figure 33a). In a later design directed at minimizing the insulating layer thickness to reduce the device final stiffness, the gap between intended PPy deposition area and the sensor area was made wider to account for lateral PPy growth as illustrated in Figure 33b.

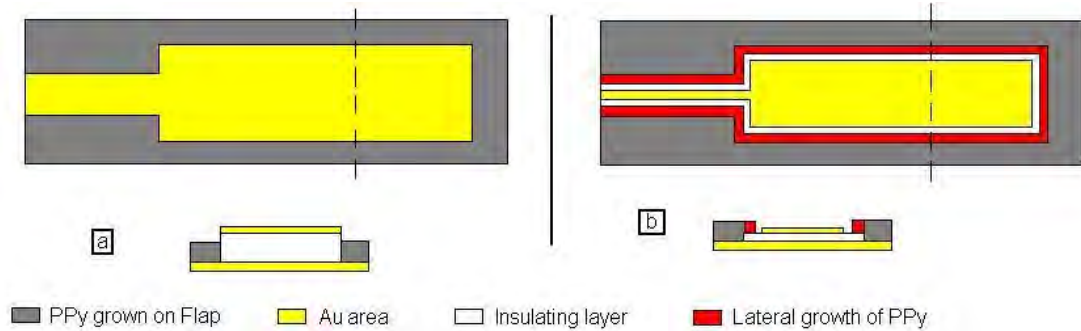


Figure 33: Fabrication strategies for thick and thin electronically insulating layers

The initial devices were fabricated as shown in Figure 33a, with both, SU-8 and Polyimide with thicknesses ranging from 4 to 20 μm used as insulating layers,. A device of this type can be seen in Figure 34.



Figure 34: SoF device

When it was obvious that the stiffness of these devices should be reduced in order to have a satisfactory movement amplitude (see 5.2.5 below), a new set of devices, as in Figures 22 and 33b, aimed at minimizing the insulating layer thickness was fabricated, this time only on Polyimide, which is a less stiff material than SU-8 and ideally it could also be made very thin.

With Polyimide the fabrication process was found to be more complicated than expected due to the difficulty of patterning well-defined shapes of thin Polyimide layers. The *undercut* suffered during Photoresist development was more pronounced for thinner Polyimide layers. Very thin layers of Polyimide were more vulnerable to discontinuities that could compromise electric insulation – issue especially severe

when Polyimide layer was covering topology with sharp edges, as presented in Figure 35.

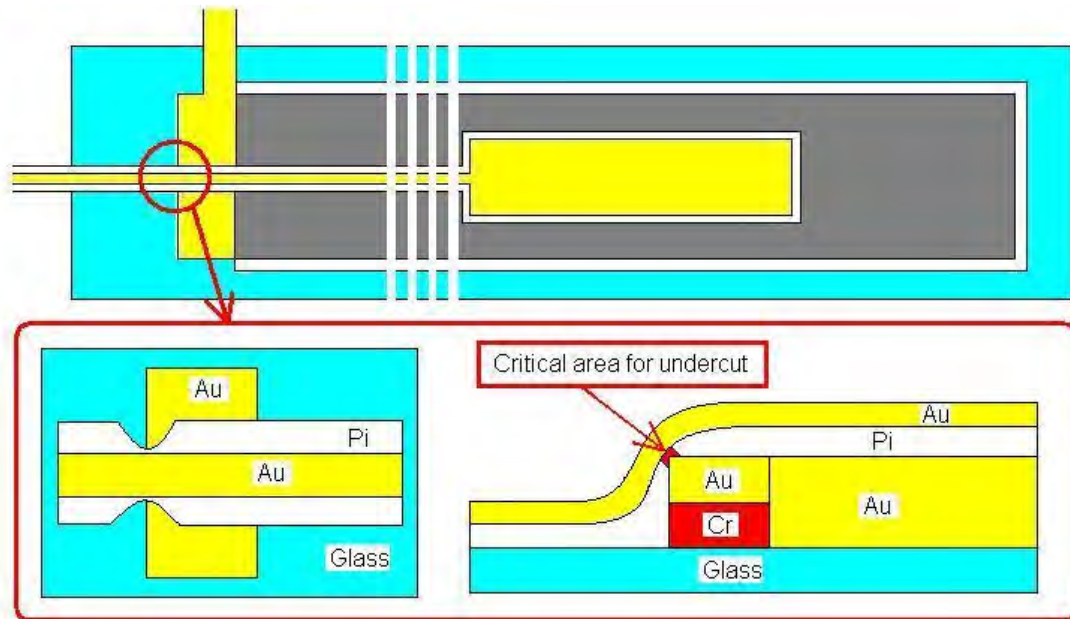


Figure 35: Undercut problems in thin Polyimide Insulating layers

When the thickness of the Pi layers was below $3\mu\text{m}$, the undercut effect was almost always enough to expose part of the underlying Au of the flap circuit to the subsequently deposited Ti/Au layers of the sensor, creating the undesired electrical contact between the two conducting elements.

It was also important to carefully control the PPy deposition process in order to avoid excessive lateral PPy growth that could reach the sensor area and create a short circuit between the Flap and the Sensor.

None of the devices fabricated in this fashion within the time frame of this study met the necessary electrical insulation condition. Some examples made with thin Pi layers as insulating material are presented in Figure 36, where it can be seen that PPy is present on both, the Flap area and the Sensor area.

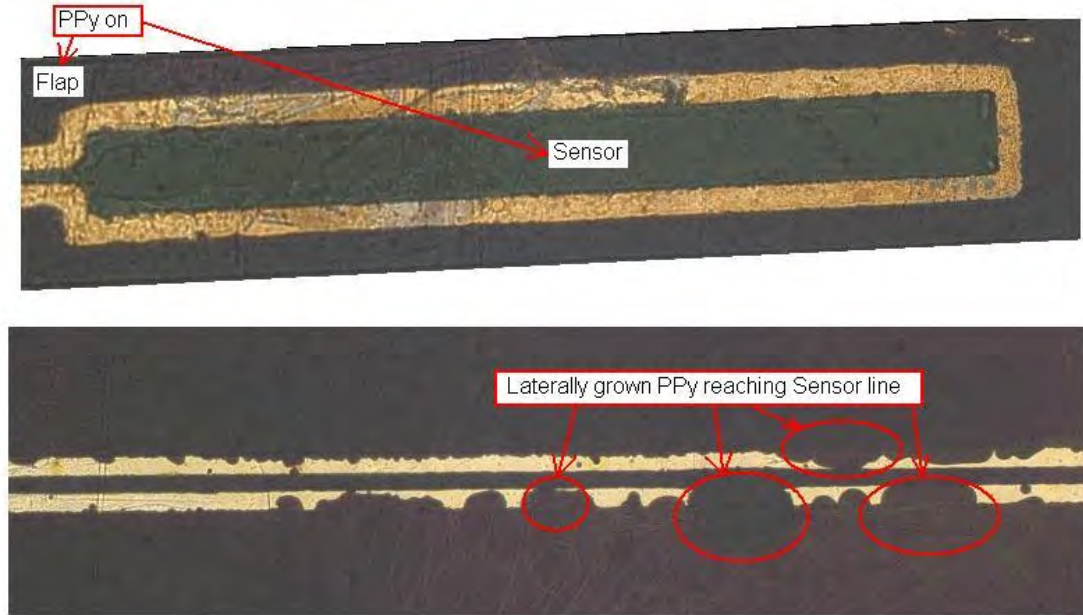


Figure 36: Undesired PPy growth on sensor area

PPy thicknesses grown on the flaps ranged from 2 to 5 μm .

5.1.3 Micro sensor near Flaps (*mSnF*)

As introduced during the last chapter, the different configurations (*1vs1*, *3vs3*, *2 On-Phase* and *6 On-Phase* Flaps configurations) of *mSnF* devices were fabricated.

The Au layer of the flaps for all configurations was fabricated in 5 different thicknesses: 30, 50, 100, 200 and 300 nm, with the additional aim of correlating the stiffness of the flap (related to the Au layer thickness) with the flap amplitude and frequency of movement.

The PPy electrochemical deposition for these devices was always performed at 0.5V, for several minutes. Larger currents than initially expected were achieved when depositing PPy on these micro-size structures (from 50 to 250 μA when depositing on all flaps of a given sample, which typically included 6 spots, at the same time),

possibly due to non-linear diffusion effects. Thus, this step needed to be carefully controlled in time in order to obtain the desired PPy thickness in each of the different samples (30, 30, 100, 200 and 300 nm Au thickness), trying always to maintain the 1:10 ratio between Au and PPy thicknesses of the flaps.

In the Figure below (Figure 37) some examples of this deposition process are shown, for samples either with two or six Flaps (2F or 6F, respectively). The average Charge needed to deposit 1 μ m of PPy was calculated to be around 0.014C.

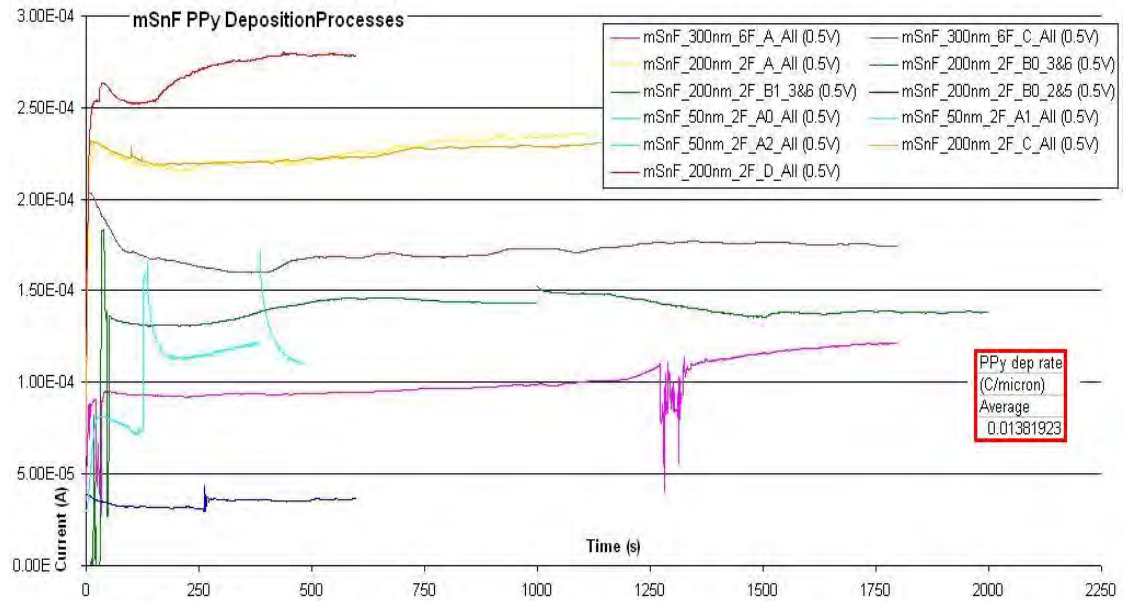


Figure 37: PPy deposition process examples

5.2 Flaps Actuation

From the experience of actuating a wide variety of devices, the following results have been observed regarding Flap actuation properties.

5.2.1 Effect of Flap dimensions on Motion

The flaps that proved to work best were the ones that approached a ratio of Au/PPy thickness of 1:10. With thicker PPy layers, PPy would grow around the flap and on the glass substrate, becoming attached to it and preventing operation of the final device. Thinner PPy layers, would not be able to exert a sufficiently large stress on the device to detach it from the substrate, and PPy would crack before actuation was observed.

The effect of length and width of the flaps on their movement is presented in section 5.2.3.

When the Au layer of the flaps was made thinner than 50nm, their continuity was compromised: small breaches and areas of poor Au deposition could be observed. This was likely due to limitations of the e-beam thermal deposition method used to deposit Au.

5.2.2 Input Function effect on Flap position

When a steady positive DC Voltage was applied on the flaps, they would assume a specific position, with each particular position corresponding to a particular voltage applied. This applied voltage – flap position correlation was observed for both voltage increase (to activate the flap) and for voltage decrease to bring the flap back to its original position.

Once the DC Voltage was relieved, the flap would recover its initial flat position.

Flap movement under the sinusoidal applied Voltages is described in the following section.

5.2.3 Flap motion model

Before the presented devices were fabricated, some initial experiments were run with flaps of various dimensions to study the motion characteristics of the Au/PPy devices that we were able to manufacture. These initial experiments were also run to verify that the experimental setup (PPy deposition equipment, Function Generator, etc.) was adequate to run the future experiments.

After testing these initial flaps and all the later fabricated devices with a wide variety of different flap characteristics and sizes, an approximate model on how the flaps move was generated.

The model was constructed for flaps of a length/width ratio between 20:1 and 10:1, lengths from 1cm to 380 μ m, PPy/Au thickness ratio of 10:1, and Au thicknesses of 300 to 100 nm.

Flaps with smaller length/width ratios tended to exhibit a high degree of “twisting” secondary motion as shown in Figure 38a, while flaps with larger length/width ratios tended to curl several times on themselves into a spiral “corkscrew” shape, as in Figure 38b.



Figure 388: Secondary “Twisting” and “Corkscrew” motions

The regular flap motion model is presented in Figure 39.

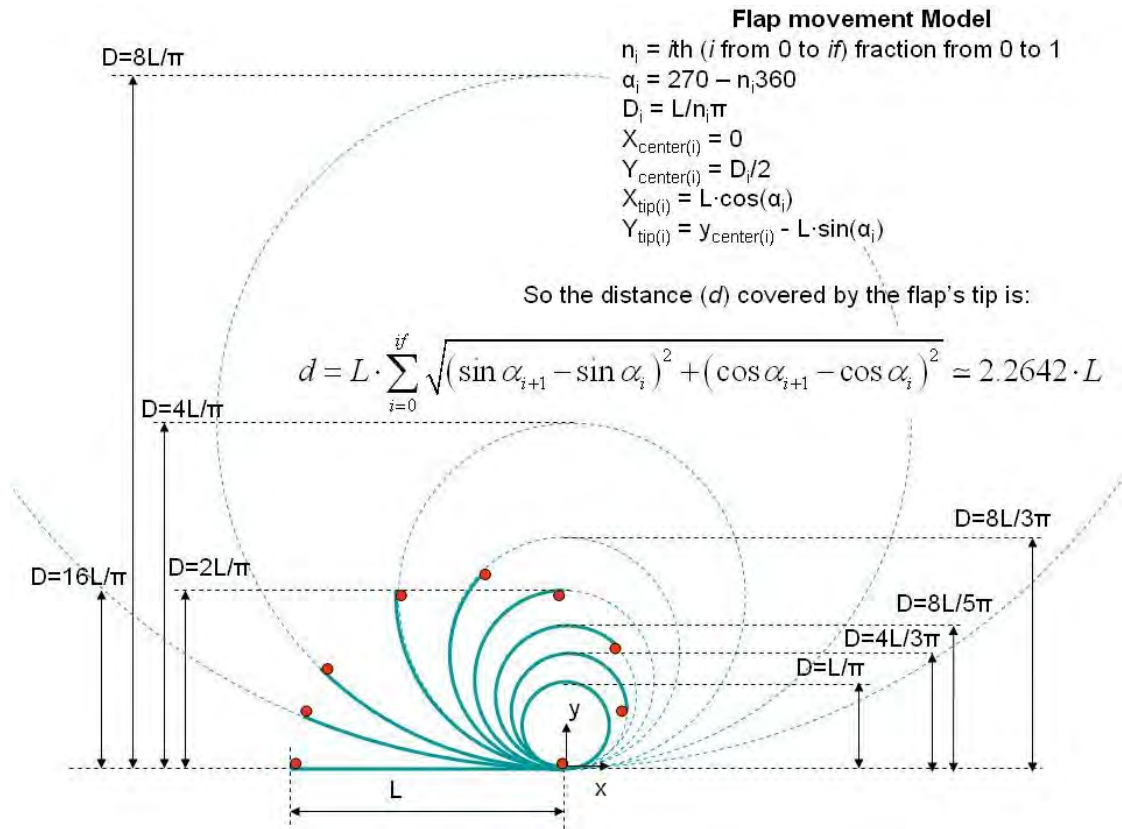


Figure 399: Flap motion model

5.2.4 Time and applied function effects on Flap motion

It was observed that when the flaps were actuated with the same applied function for a certain amount of time (depending on the flap's characteristics), a general tendency of all flaps was to lose their ability to recover the initial flat position. The longer the flaps were actuated, the further away from their starting position they would finally be moving (Figure 40a), progressing over time towards a fully contracted and motionless final stage.

This effect was observed to progress more rapidly when the flaps were actuated at higher Amplitudes and Frequencies.

Another observation was that when increasing the sinusoidal function Amplitude, the flaps would cover larger distances. Therefore, when after being actuated for a certain time the flaps wouldn't recover their initial position, a sufficient increase in the function's Amplitude would usually allow them to move back again to the initial flat position (Figure 40b).

Finally, it was also seen that when the Frequency of the sinusoidal function was increased, the flaps would move faster, but their movement amplitude would decrease and their position would be further away from the flat initial stage (Figure 40c).

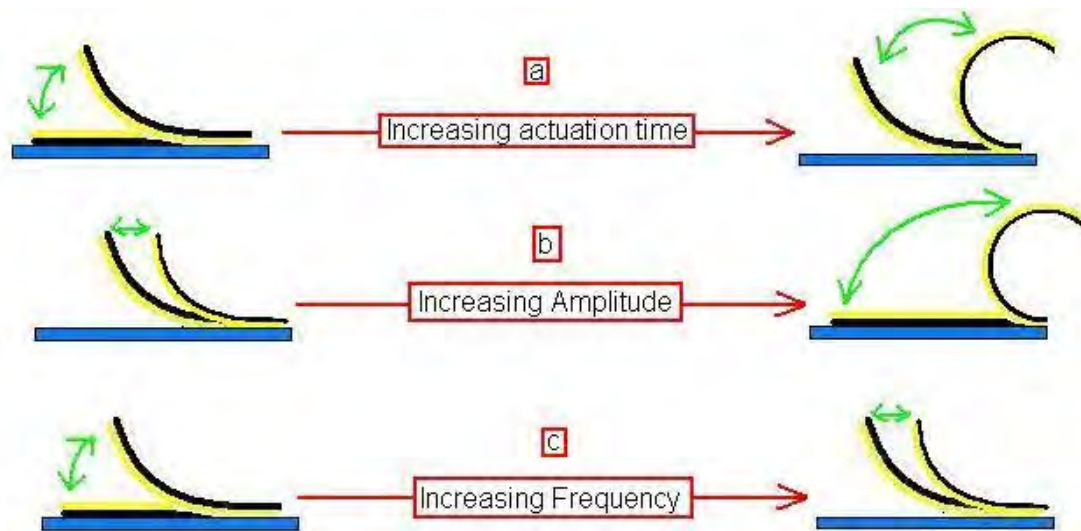


Figure 40: Effects of time and applied function on the motion of the flaps

5.2.5 Flap motion in the devices tested

For the *SnF* experiments, the observed motion of the flaps was similar to that indicated in section 5.2.3. Detailed examples will be presented coupled with *ChA Mixing* experiments in the next section. This will be done with the aim that by observing the flaps motion during the *ChA Mixing* experiment, the characteristics of

the flaps motion could be associated with any possible increased mass transport effects (directly related to any increase in the sensor signal).

For the *SoF* experiments the observations will be presented the next section as well. As mentioned previously, the initial *SoF* devices (which were made with 4-20 μm thick insulating SU-8 and Polyimide layers) were usually too stiff to develop a high amplitude/high frequency flap movement. In the next section a *Mixing* experiment will be presented for one of these devices that, presenting good electrical insulation, also had the highest movement amplitude among these devices (although it was significantly less than the amplitude observed in the SnF devices).

A later *SoF* device (with thin, 3 μm thick, Polyimide insulating layer) is presented in Figure 41.

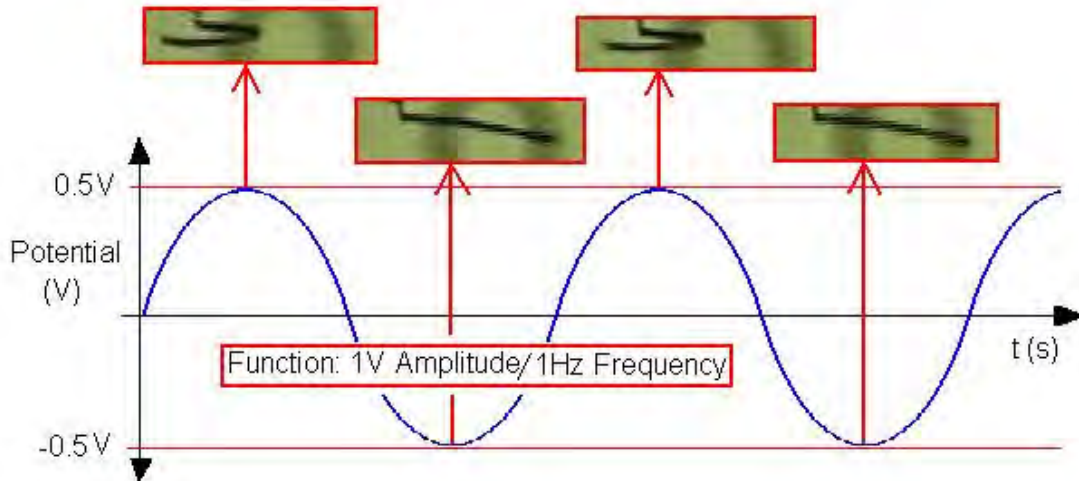


Figure 41. Movement of a *SoF* device with 3 μm thick Polyimide insulating layer

Since PPy is present on the sensor, electrically connecting it with the flap, this device can't be used in *Mixing* experiments. Nevertheless these results demonstrate that with sufficiently thin insulating layers (below 3 μm) a high movement amplitude can be achieved, and therefore new materials with low stiffness and more reliable fabrication processes should be explored as insulators.

For the *mSnF* devices, ChA *Mixing* experimental results coupled with recorded flap movement will also be shown in the next section. Depending on the deposited PPy quality, some devices could be actuated without the need of the Polyimide addition layer as Au would detach from the Glass substrate (as reported in the literature [25]). However, in all cases the existence of a Polyimide layer facilitates flap detachment.

Another observation was that flaps with 200 nm thick Au layer generally worked better (larger amplitudes and higher frequencies) than flaps with 300nm thick Au layer (100nm and 50nm Au thick flaps not checked yet).

5.3 Electrochemical experiments

5.3.1 Notes on experimental set-up

During the period when the *mSnF* devices were tested the Gamry Femtostat seemed to behave erratically in some tests (due to an unexplained saturation of the recorded signal). Other issues of the experimental setup included: bad contact between the alligator clips joining the samples with the Potentiostat and the Function Generator; some samples did not have a well deposited Pi layer insulating the contact lines of the Sensor area from the solution, etc.

For these reasons many experimental results had to be discarded as possibly invalid. The remaining results are reliable, but nevertheless some future additional experiments designed to demonstrate repeatability of these experiments would be desirable. Thus, the results presented in this work should be regarded as preliminary data.

5.3.2 Current-Potential (*i*-*E*) Experiments

The data collected as from these experiments is presented in the I-E curve illustrated in Figure 42.

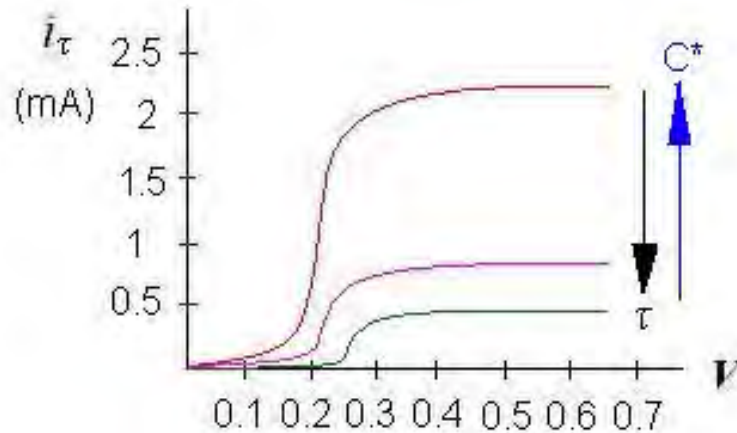


Figure 42: *i*-*E* curve for $Fe(CN)_6^{4-}$ in PBS

The diffusion-limited plateau of the *i*-*E* curve for the oxidation of $Fe(CN)_6^{4-}$ begins around 0.3V. Thus, a 0.4V (and sometimes 0.5V) was established as the standard potential at which the ChronoAmperometric experiments were to be performed, so that the response of the sensor would solely be a mass transport dominated process (and any relevant mass transport effects caused by the moving flaps on the fluid surrounding the sensor could be detected).

5.3.3 ChronoAmperometric Experiments

As explained before in sections 4.3.2 and 4.3.3, three types of ChA experiments under different conditions were performed: *Diffusion-limited Blanks* (without any interferences and without any flap activity), *Noise Blanks* (with interferences but

without flap activity), and *Mixing* experiments (with both, interferences and flap activity).

The results of these experiments for the different flap configurations tested (*SnF*, *SoF*, *mSnF*) are presented and discussed below.

5.3.3.1 *Diffusion-limited Blank and Noise Blank experiments*

Before conducting the *Mixing* experiments (ChA on the sensor plus flap actuation), *Diffusion-limited Blank* and *Noise Blank* experiments were conducted (as presented in the last chapter), to test the validity of the assumption that the interferences are added to the mass transport-limited signal.

Some illustrating results obtained during these experiments for the 3 different configurations are presented in the figures below. In addition to the mentioned results, the figures also include the results of the numerically treated *Noise Blank* experiments.

For the *Sensor near Flap (SnF)* devices, a typical experimental result can be observed in the following Figure 43.

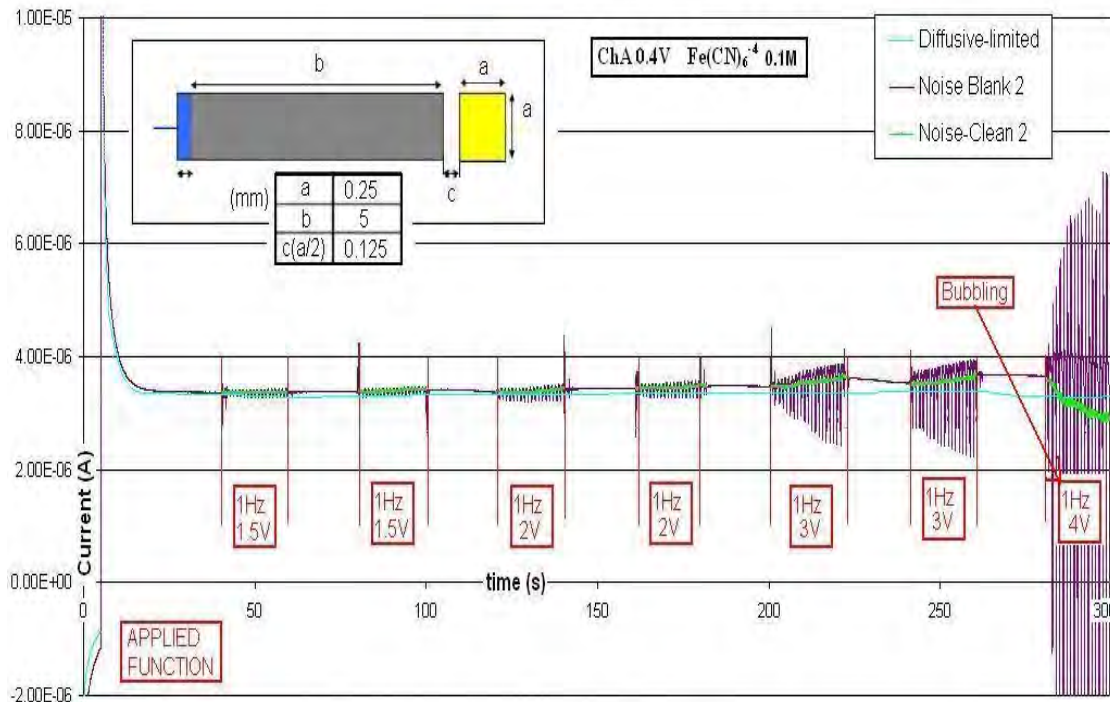


Figure 43: Noise Experiment for a SnF device

In this experiment the smallest *SnF* device was used. Thus, the distance between the interfering electrode and the sensor was the minimum for this set of devices, so the largest possible interference was experienced. In the ChA experiment presented, a sinusoidal function was applied on the interfering electrode with different Amplitudes and Frequencies (purple line). As can be seen from Figure 43, for applied bias of less than 3V, treatment with the numerical methodology to remove interferences (as described in Section 4.3.4) produced a signal (green line), identical in shape to the *Diffusion-limited* experiment (blue line).

For Amplitudes of 3V and higher, the interference becomes more complex and it cannot be treated as simple periodical signal that builds up on the mass transport-limited underlying signal. In addition, when hydrolysis takes place, as for the given example at 4V Amplitude, some additional interfering phenomena (mass transport due to bubbling and new redox species formation) can alter the sensor readings.

For the *Sensor on Flap (SoF)* configuration, tests were conducted on devices that were successfully insulated (for insulating layers thicker than $4\mu\text{m}$, either in SU-8 or Polyimide). In the following Figure 44, there is an example of one these experiments.

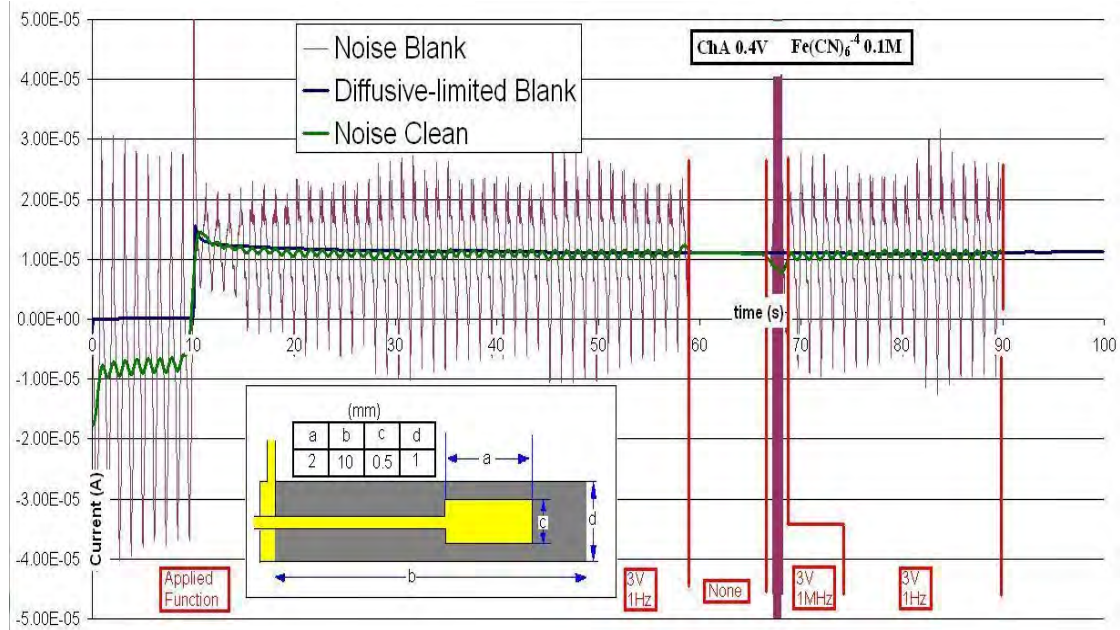


Figure 44: Noise Experiment for a SoF device

The tested device was fabricated with an insulating layer of SU-8 of $10\mu\text{m}$. For applied bias of up to 3V, the ChA response of the sensor (purple line) filtered with the numerical methodology described above (green line), matched the *Diffusion-limited Blank* experiment response (blue line). It should be noted that under these conditions some bubbling was observed on the flap, but this didn't seem to affect the sensor reading (that was situated $10\mu\text{m}$ away from the reaction promoting electrode).

For the *Micro sensor near flaps (mSnF)* devices, a typical result is given in Figure 45.

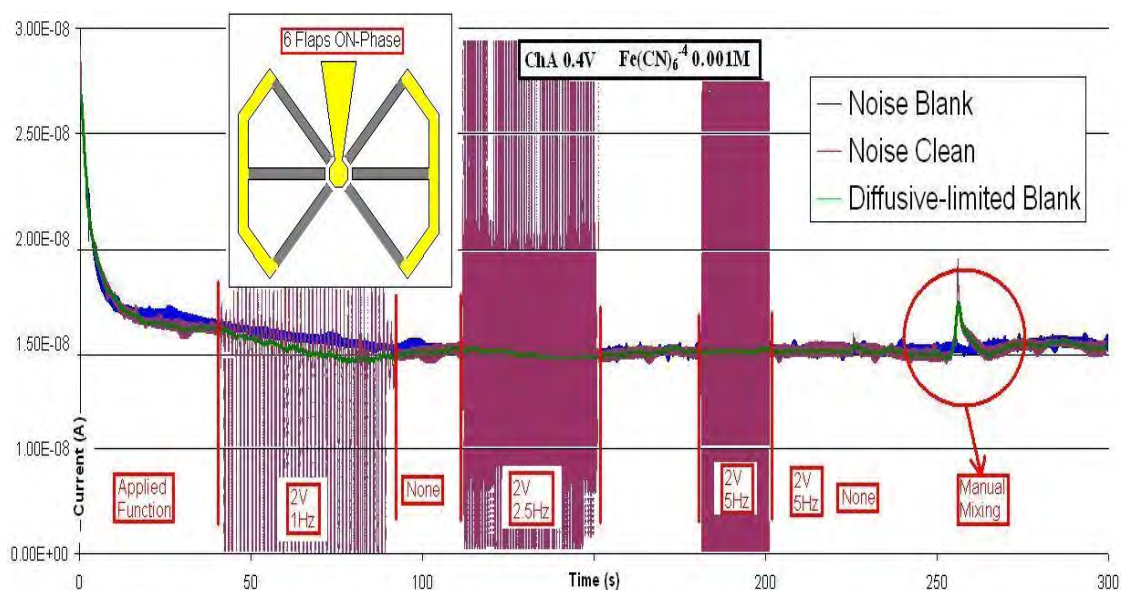


Figure 45: Noise Experiment for a mSnF device

Similarly to the experiments described above, the *Noise Blank* experiments, after treating the signal with the numerical method, had the same shape than the *Diffusion-limited Blank* experiments if the applied bias did not exceed certain values (in the presented case 2V Amplitude and 5Hz Frequency).

These experiments prove that, under certain limitations, the interference that affects the sensor readings can be removed. It is worth mentioning that these experiments were all performed with interfering electrodes located as close as possible to the sensor. Thus, all possible interferences (EMI and Redox) are maximized during these experiments. If it is proven here that they can be removed for the *Noise-Blank* experiments, the same should also be valid for the *Mixing* experiments (with the considerations introduced below).

It is important to note that during flap actuation the interfering electrodes will be in the closest proximity to the sensor (and thus creating maximum EMI and Redox interferences) when the applied bias is Negative, while at Positive bias they will be contracted and so far away from the sensing area with which they interfere. Therefore

it is possible that Negative Potentials induce more pronounced interferences than when Positive Potentials are applied.

Thus, for EMI effects (that are very sensitive to distance), this means that Negative applied potential will have larger effect than the Positive potential (because the flaps are closer to the sensor), and so a possible Negative drift will be induced in the sensor signal.

Regarding Redox effects, Positive Potentials on the flaps will promote oxidation of $\text{Fe}(\text{CN})_6^{-4}$ to $\text{Fe}(\text{CN})_6^{-3}$ (as happens on the sensor), while Negative potentials will promote the opposite reaction. Thus when the flaps are close to the sensor, the species reacting with the sensor will be produced, and this could increase the sensor's signal. Nevertheless $\text{Fe}(\text{CN})_6^{-3}$ is not initially present in the solution and it is only created on the sensor's surface, while $\text{Fe}(\text{CN})_6^{-4}$ is the only initial species present in the solution. Then the maximum effect of the interfering electrode could only be to maintain $\text{Fe}(\text{CN})_6^{-4}$ at its initial bulk concentration (but never higher), a condition that we assume for all regions except for the *Diffusion Boundary layer*, which could certainly be modified due to this Redox interference in the *mSnF* devices. But if this was to be the case, and the presence of the interfering electrode would interfere with the *Diffusion Boundary layer* so to maintain it closer to the Bulk concentration, a Positive Dirft in the "Clean" *Noise-Blanks* with respect to the *Diffusion-limited Blanks* would already had been observed. Because this was not the case, although the fact that this interference could be maximized during flap motion as explained before, the positive drift-effect that this interference would possibly have on the future *Mixing* experiments will be disregarded as irrelevant to the final results.

To summarize, only a Negative drift could be induced during the *Mixing* experiments as a result of EMI interference due to the motion of the flaps. Therefore, the interference could only act by **reducing** the current signal obtained during the *Mixing* experiments. The conclusion is that the reported results of the *Mixing* experiments are conservative (i.e. at least as good as reported below).

5.3.3.2 Mixing experiments

In this chapter the most relevant experimental results will be presented for each of the all the device configurations fabricated.

SnF Mixing Experiments: The ChA response of the sensor, coupled with the flap position at different times during the most relevant two experiments is presented in Figures 46 and 47.

As can be seen, the effect of a single flap (with dimensions of 10x0.5mm in Figure 46 and 5x0.25mm in Figure 47) can add up to a 100% of the initial Diffusion-limited signal.

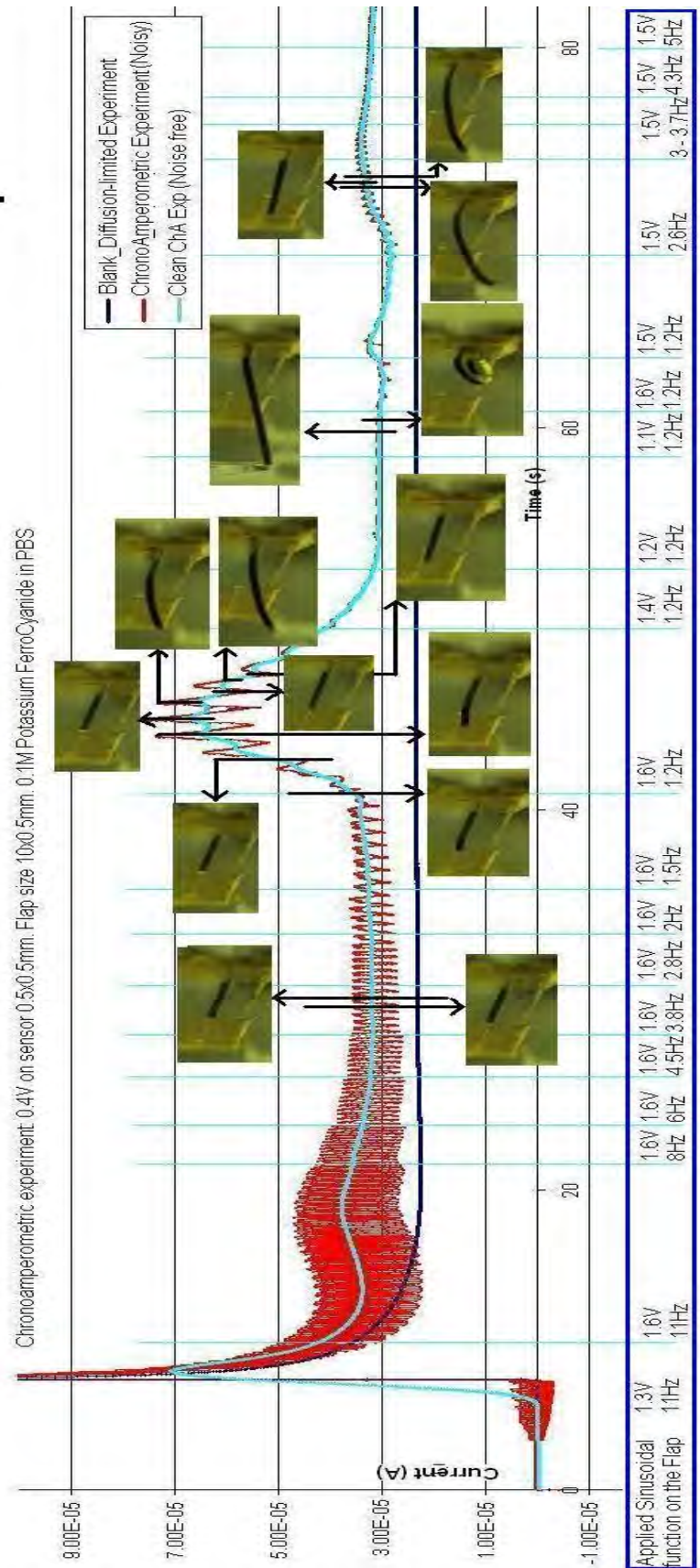


Figure 46: Mixing experiments for a SnF (10x0.5mm)

From the previous experiments it can be readily seen that when the flap was either motionless or moving away from the sensor area, the signal on the sensor was only affected by periodic effects. However, when the flaps moved at high amplitudes and they returned to their initial flat position on every cycle, it was observed that the signal on the sensor (after the periodic interference is removed), was no longer fitting the signal of the previous *Diffusion-limited Blank* experiments. Therefore, we propose that the increase in the sensor signal was due to effective *mixing* created by the flaps motion.

SoF Mixing Experiments: The best movement results (for successfully insulated devices) were achieved for flaps with 4 μm thick SU-8 insulation layer. Figure 48 shows the results of this experiment.

As it can be seen, once the periodic interference was cleaned from the Noisy signal, there was no appreciable difference between the *Diffusion-limited Blank* and the *Mixing* experiments. This means that for this particular device, the motion of the flap didn't create any substantial *mixing* effect to affect the sensor reading.

mSnF Mixing Experiments: For all the configurations of these devices (except for the *1vs1* Flaps configuration), several experiments were run. The most relevant results for each configuration are shown below: *2 On-Phase* Flaps results in Figure 49; *6 On-Phase* Flaps results in Figure 50; *3vs3* Flaps results in Figure 51.

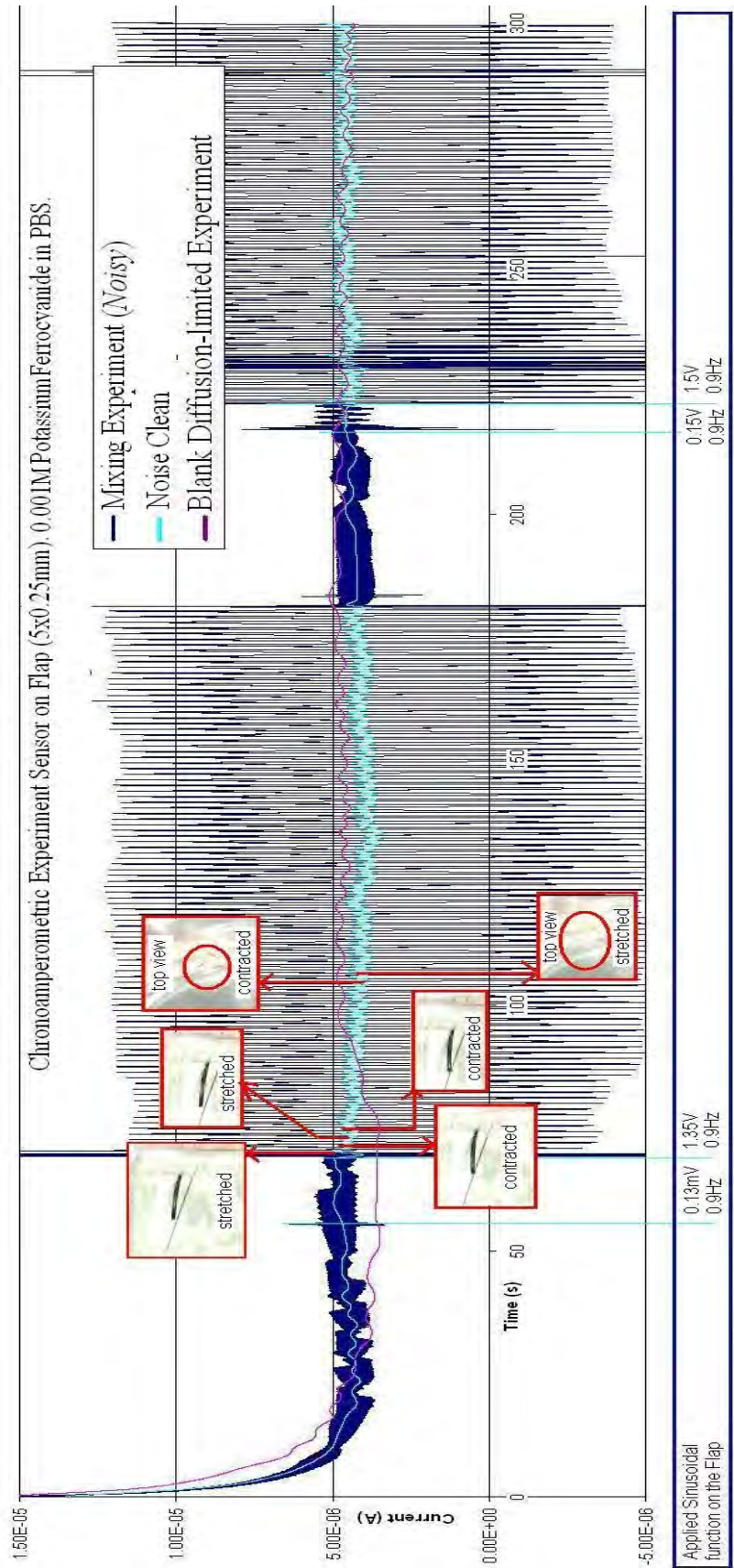


Figure 48: Mixing experiments for a SoF (10x0.5mm)

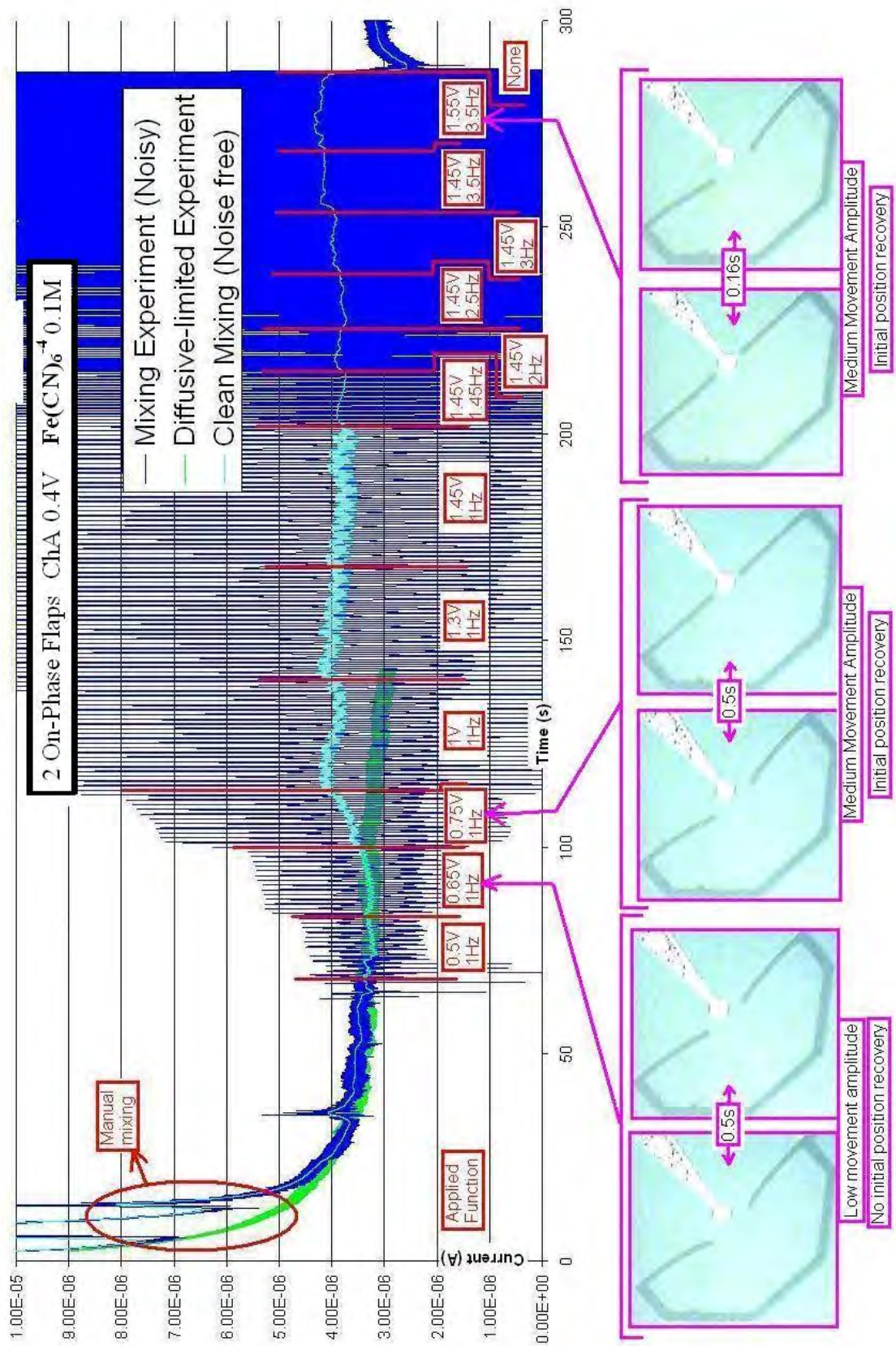


Figure 49: Mixing experiments for a $mSnF$ (2 On-Phase Flaps)

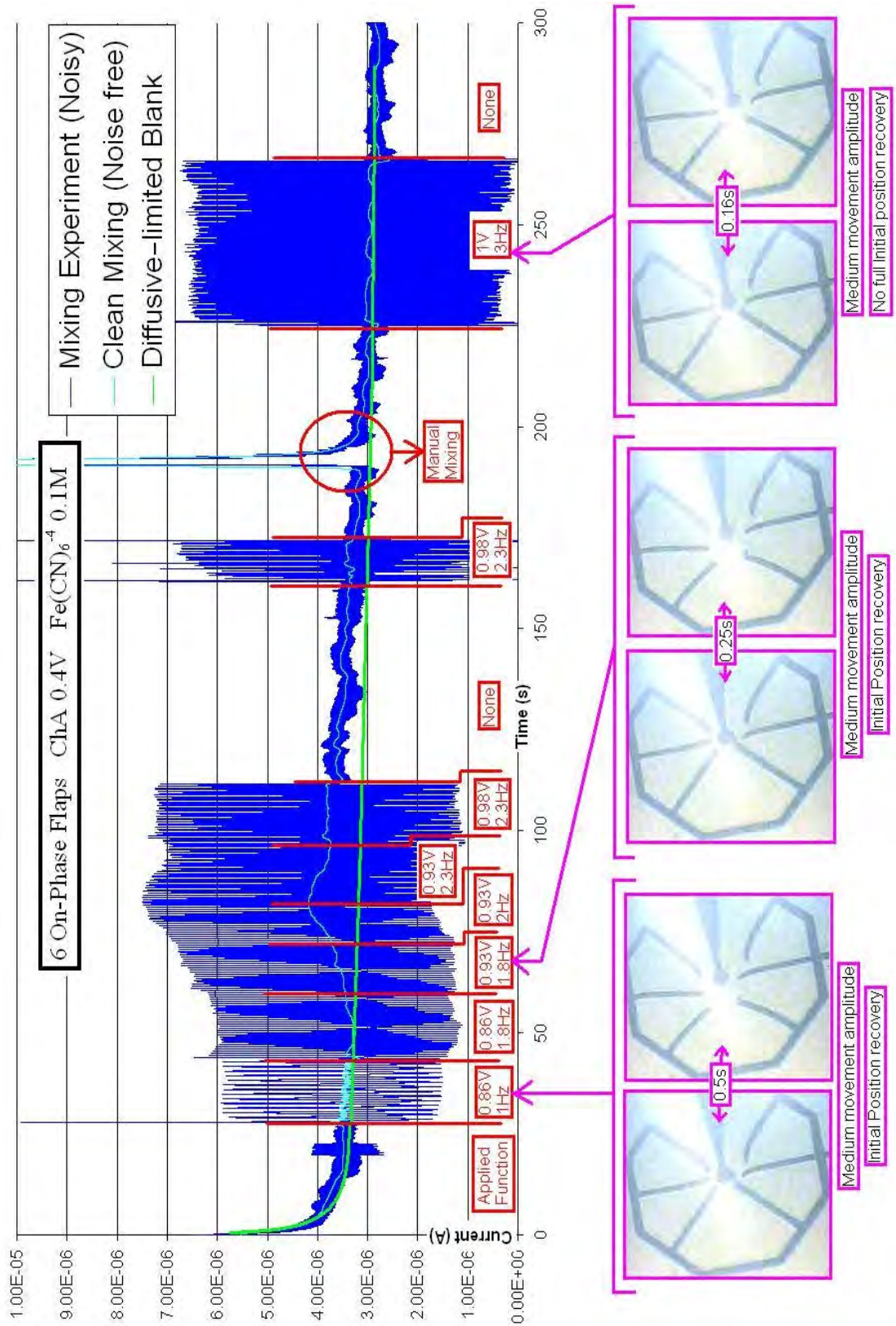


Figure 50: Mixing experiments for a mSnF (6 On-Phase Flaps)

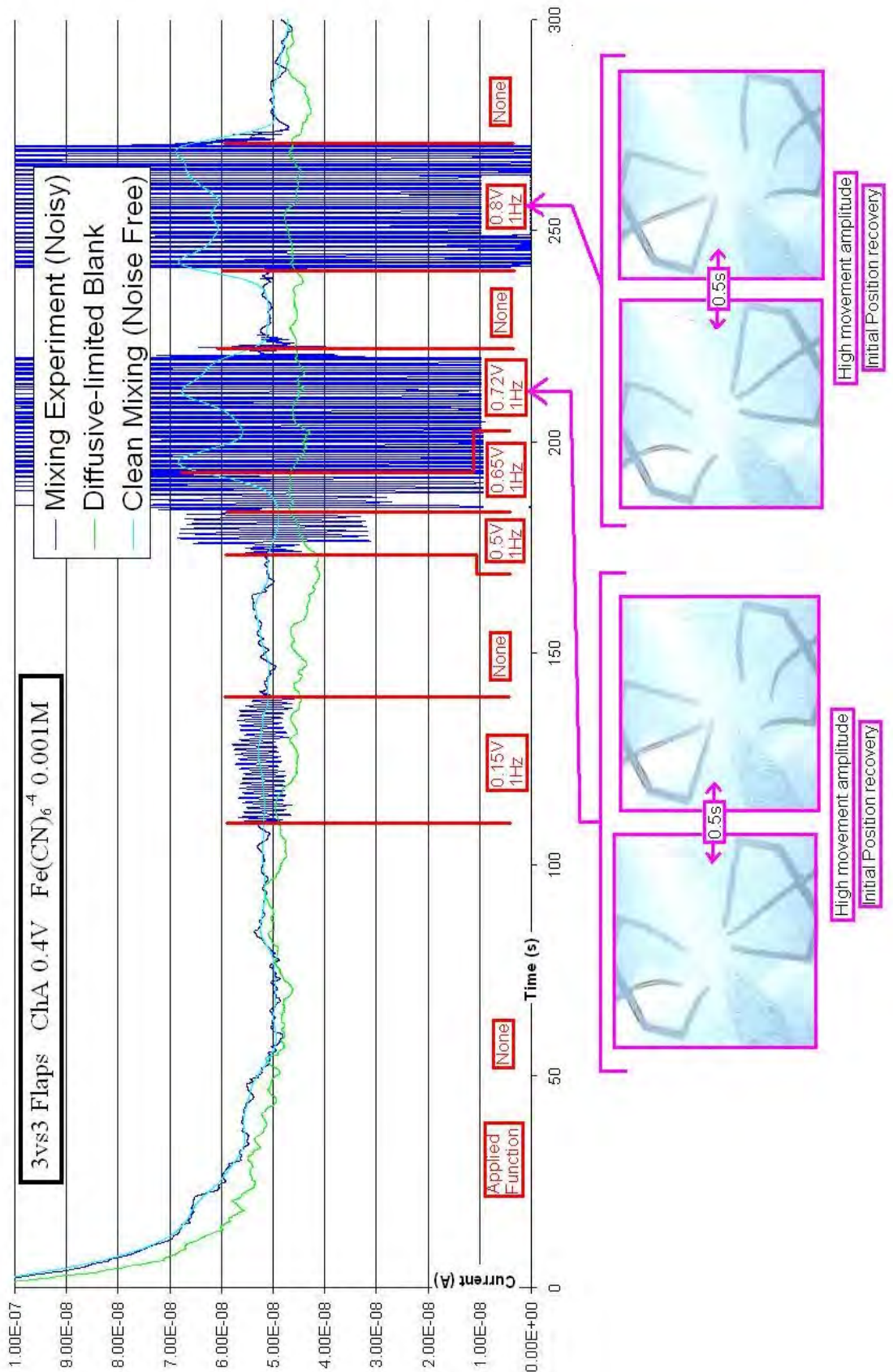


Figure 51: Mixing experiments for a mSnF (3vs3 Flaps)

None of the experiments on the *1vs1* Flaps configuration was successfully performed during the time of this study.

As can be seen from these experiments, the presence of the actuating Flaps increased the *Diffusion-limited Blank* signal. For the *2 On-Phase* and *6 On-Phase* Flaps configurations, the maximum increase observed was approximately **30%**. For the *3vs3* Flaps device, the increase was up **40%** with respect to the Diffusion-limited signal.

It must be noted that for the two first experiments the concentration of $\text{Fe}(\text{CN})_6^{-4}$ was 0.1M, and for the last experiment it was 0.001M. Nevertheless, the results are comparable due to the direct relationship to the bulk Concentration (C^*) of both, the Diffusion-limited current (Cottrell experiment), as in eq. (21), and the Convective term of eq. (20). Thus the current of the *Diffusion-limited Blanks* and the *Mixing* experiments is directly proportional to C^* . As long as these two experiments are run for the same $\text{Fe}(\text{CN})_6^{-4}$ concentration, this factor is only relevant for issues like the limit of detection of the experimental apparatus.

It must also be pointed out that the *Diffusion-limited Blank* experiments don't perfectly match the theoretical results of the Cottrell experiment. This is a consequence, as mentioned previously, of some convective effects experimented as intrinsic "noise" of the *Diffusion-limited* tests, due to environmental vibrations. Thus, the added signal due to mixing with the tested actuators that has been observed, would probably be much more relevant if this intrinsic noise of the *Diffusion-limited* experiments could be avoided.

Nonfaradic effects also add up to the results presented, as introduced in eq. (15), but their importance is minimal and can be neglected for the cases where comparisons between two identical electrochemical experiments (but for different mass transport phenomena) are made.

Another issue worth mentioning is that the size of the sensors (octagons of $38\mu\text{m}$ side), is almost reaching the size of UME (Ultra Small Electrodes), which are typically under $25\mu\text{m}$ radius. This might also cause an increase in the expected Diffusion-limited signal due to non-linear diffusion, and thus a larger deviation from the ideal Cottrell behavior.

Also, the sensing area in most of the experiments was larger than the initially designed octagonal sensor. This happened due to a design flaw (discovered while testing the final devices) in the fabrication process, that prevented the use of a good insulating (thick) layer of Pi on the contact lines of the sensor. Because of this, a partial area of the sensor's contact lines was almost always exposed to the solution and so it could also participate in the Redox process. For this reason the Diffusion-limited current obtained (proportional to the available area of submerged WE) was probably larger than would be desirable and the Mixing effects picked up on only a portion of this area (the octagonal sensor) could be cut down when compared to their relevance if only the smaller octagonal sensor area had been available for reaction. In most cases this extra sensing area was even bigger than the octagonal sensor area itself, and so the final "sensing system" was less susceptible to the Mixing action of the flaps. Therefore, a more pronounced *mixing* effect would have been observed if a good insulation of the sensor contact lines had been achieved.

Similarly, as in the *SnF* experiments, it was also observed that two critical conditions that needed to be met so that the sensor response of the *Mixing experiments* would be improved when compared to the *Diffusion-limited experiments* were: The flaps need to have a large movement amplitude and also they have to recover the initial flat position. When these two conditions were met, it was also seen that higher frequencies of movement would further increase the *mixing* effects.

6 Conclusions

The results presented in this study demonstrate that when properly fabricated and actuated, the Au/PPy flaps are capable of achieving active Micromixing, increasing diffusion-limited mass transport by as much as a 40% in the particular systems tested.

As explained in the results section, the mass transport increase due to *Active Micromixing* with these devices is possibly even higher than here reported. Suppressed current readings of the sensor could be due to the EMI Negative-drift, the extra sensing area indifferent to mixing and the environmental noise in the apparatus set-up.

Another fact that should be considered is the “semi-infinite” approach used in these experiments: the analytical Redox method used relied on a large excess of analyte in the medium (large beakers of solution) the abundance of which could be considered “semi-infinite”. In a “finite” approach (as, for instance, a microchamber with very limited volume and amount of analyte), increase in the diffusion-limited mass transport would very likely be even more relevant.

The advantages of the proposed *Active Micromixing* approach are its capability for effectively creating *Micromixing*, a very low Voltage source needed for the actuation of the device, and its ability to mix in small, isolated volumes without the need to pass fluids through long microchannels.

7 Future Work

Future work will involve optimization of the described micro-mixers. Simulation of actuating multi-flap devices with the available PDE multi-physics solvers will be performed with the aim of creating the most effective flows that would promote Chaotic Advection so to maximally enhance *Micromixing*.

Some improvements (already outlined in this document) will be made to the experimental setup. The “finite”-case studies will be performed and the direct use of these mixing devices in current micro-reaction applications (for instance DNA detection hybridization-based reactions) will be implemented.

REFERENCES

- [1] Kumar Khanna; “Biotechnology Advances”, vol 25, 2007, 85-98
- [2] Panescu; “IEEE Engineering in Medicine and Biology”, vol 25, 2006, 19-28.
- [3] Dittrich et al; “Nature reviews Drug Discovery”, vol 5, March 2006, 210-218.
- [4] Eaton et al; “Structure”, vol 4, October 1996, 1133-1139.
- [5] Knight et al; “Physical Review Letters”, vol 80, April 1998, 3863-3866.
- [6] Heule et al; “Lab on a Chip”, vol 4, 2004, 506-511.
- [7] Toegl et al; “Journal of Biomolecular Techniques”; vol 14, 2003, 197-204.
- [8] Cunningham; “Analytica Chimica Acta”; vol 429, 2001, 1-18.
- [9] Beebe et al; “Annual reviews on Biomedical Engineering”; vol 4, 2002, 261-286.
- [10] Nguyen; “Annual reviews on Biomedical Engineering”; vol 4, 2002, 261-286.

- [11] Purcell; "American journal of Physics", vol 45, 1977, 3-11.
- [12] Kamholz et al.; "Analytical Chemistry"; vol 71, 1999, 5340-5347.
- [13] Weigl et al; "Science", vol 283, 1999, 346.
- [14] Baroud et al; "Physical Review E", vol 67, 2003, 060104.
- [15] Hatch et al; "Natural Biotechnology", vol 19, 2001, 461.
- [16] Brody et al; "Biophysical Journal"; vol 71, 1996, 3430.
- [17] Brody et al; "Sens. Actuators, A", vol 58, 1997, 13.
- [18] Cho et al; "Analytical Chemistry", vol 75, 2003, 1671.
- [19] Schilling et al; "Analytical Chemistry", Vol 74, 2002, 1798.
- [20] Aref et al; "Physics of Fluids", vol 14, 2002, 1315.
- [21] Stroock et al; "Science", vol 295, 2002, 647.
- [22] Stroock et al; "Philosophical Transactions of the Royal Society, Ser. A", vol 362, 2004, 971.
- [23] Ottino, J. M., 1989, "The Kinematics of Mixing: Stretching, Chaos, and Transport (Cambridge University Press, Cambridge, England).
- [24] Glasgow and Aubry; "Lab Chip", vol 3, 2003, 114.
- [25] Nguyen et al; "Journal of Micromechanics and Microengineering", vol 15, 2005, R1-R16.
- [26] E. Smela; "Advanced Materials", vol 15, 2003, 481.
- [27] E. Smela; "Journal of Micromechanics and Microengineering", vol 9, 1999, 1-18.
- [28] Smela et al; "Science", vol 268, 1995, 1735.
- [29] Madou et al; "Journal of Smart Materials and Structures", accepted 09/2006.
- [30] Ottino; "The kinematics of mixing", Chap. 2, Cambridge University Press, 1989.